Geochemistry, Geophysics, Geosystems®

RESEARCH ARTICLE
10.1029/2025GC012357

Key Points:

- We develop a geochemical model to quantify mantle source parameters from the global radiogenic isotope systematics of oceanic basalts
- Geochemical and geodynamical model runs agree quantitatively plumes have excess peridotite depletion and recycled crust compared to ridges
- Cross-comparison of models constrains core-mantle boundary parameters, buoyancy number, and early mantle differentiation parameters

Supporting Information:

Supporting Information may be found in the online version of this article.

Correspondence to:

P. Béguelin,
BeguelinP@cardiff.ac.uk

Citation:

Béguelin, P., Panton, J., Andersen, M., Elliott, T., Davies, H., Rodney, J., & Plimmer, A. (2025). Comparing geochemical and geodynamical models of plume and ridge mantle source composition. *Geochemistry, Geophysics, Geosystems*, *26*, e2025GC012357. https://doi.org/10.1029/2025GC012357

Received 7 APR 2025
Accepted 11 JUN 2025

Author Contributions:

Conceptualization: Paul Béguelin, James Panton, Morten Andersen, Tim Elliott, Huw Davies, Joel Rodney
Data curation: Paul Béguelin, James Panton, Abigail Plimmer
Formal analysis: Paul Béguelin, James Panton
Funding acquisition: Morten Andersen, Tim Elliott, Huw Davies
Investigation: Paul Béguelin, James Panton

Comparing Geochemical and Geodynamical Models of Plume and Ridge Mantle Source Composition

Paul Béguelin[1], James Panton[1], Morten Andersen[1], Tim Elliott[2], Huw Davies[1], Joel Rodney[2], and Abigail Plimmer[1]

[1]School of Earth and Environmental Sciences, Cardiff University, Cardiff, UK, [2]School of Earth Sciences, University of Bristol, Bristol, UK

Abstract We use a multidisciplinary approach to investigate how the parameter space of mantle convection affects present-day mantle composition. We compare 22 forward geodynamical mantle circulation model simulations against 24 variants of a geochemical inversion model of the global radiogenic isotope data set of mantle-derived lavas. Both models are fully independent but able to output compositional parameters for the lower mantle sampled by upwelling mantle plumes and for the upper mantle sampled by mid-oceanic ridges. Geodynamical model results suggest an excess degree of peridotite melt-depletion $\Delta F_d = +0.4\% \pm 0.4\%$ and an excess amount of recycled crust $\Delta f_{RC} = +2.7\% \pm 3.1\%$ in plumes compared to ridges, while the geochemical inversion returns $\Delta F_d = +0.4\% \pm 1.2\%$ and $\Delta f_{RC} = +1.5\% \pm 0.6\%$. Models are thus in quantitative agreement but with opposite sensitivities, allowing to restrict their respective parameter space. Geodynamical runs show best fits with the narrow geochemical Δf_{RC} for core-mantle boundary (CMB) temperatures of 3,400–3,800 K and a recycled crust buoyancy number of 0.44–0.66. A dense primordial layer at the CMB also leads to a better fit. Variants of our geochemical model show a best fit with the narrow geodynamical ΔF_d value when early mantle differentiation occurs in the garnet stability field. We also find that the formation of early compositional heterogeneities is needed to fully explain the isotope range of mantle melts. Our work emphasizes the need to correct isotopic data for the effects of non-magmatic processes in a quantitative geochemical model before extracting the parameters relevant to a comparison with geodynamical model results.

Plain Language Summary The mantle is the solid but plastic layer that makes up most of Earth's interior. Understanding the convection of mass and heat in the mantle is relevant to many research topics, from plate tectonics to the habitability of terrestrial planets. In the present study, we compare the results of runs from two fully independent numerical models of the mantle: (a) a model exploring the effect of physical mantle parameters on the circulation of mantle material, and (b) a model calculating mantle composition from the global geochemical data set of oceanic lavas that are melts from the mantle. Both models can quantify two key variables of the mantle at the local scale: the proportion of mass lost from ancient melting events and the amount of recycled material from the Earth's crust. Results from both models yield values 0.4%–2.7% higher for these two variables in the deep mantle compared to the shallow mantle. The models are in quantitative agreement, but each is more sensitive to one variable. This allows a cross-examination of both models' variable inputs and narrows the uncertainty of a range of thermal, physical, and chemical parameters of the mantle.

1. Introduction

1.1. Mantle Convection Is an Open Problem

The mantle is our planet's most massive and voluminous reservoir. Material circulates within the mantle through convection, allowing the exchange of mass and heat between Earth's surface and its deep interior. Earth's crust is extracted from the mantle through partial melting, and crustal material is re-introduced into the mantle through subduction (Coltice et al., 2017; Davies & Richards, 1992; Korenaga, 2018). Through time, this processing creates thermochemical heterogeneities in the mantle and may give rise to large-scale density structures (Garnero & McNamara, 2008).

Modern whole-mantle seismic imaging techniques (seismic tomography) reveal dense down-going slabs, a highly heterogeneous lower mantle, and buoyant upwelling plumes that are the roots of most hotspots at the surface (French & Romanowicz, 2015; Montelli et al., 2006). The mineral chemistry of mantle-derived melts suggests systematically higher potential temperatures in mantle plumes compared to the upper mantle melting at

Methodology: Paul Béguelin, James Panton, Morten Andersen, Tim Elliott, Huw Davies, Joel Rodney
Project administration: Morten Andersen, Tim Elliott, Huw Davies
Resources: Huw Davies
Software: Paul Béguelin, James Panton
Supervision: Morten Andersen, Tim Elliott, Huw Davies
Validation: Paul Béguelin, James Panton
Visualization: Paul Béguelin
Writing – original draft: Paul Béguelin, James Panton, Huw Davies
Writing – review & editing: Paul Béguelin, James Panton, Morten Andersen, Tim Elliott, Huw Davies, Joel Rodney, Abigail Plimmer

mid-oceanic ridges (Bao et al., 2022; Herzberg et al., 2007; Li et al., 2025; Putirka, 2008). Likewise, the radiogenic isotope systematics of plume-derived melts (oceanic island basalts, OIB) and mid-oceanic ridge basalts (MORB) presents systematic differences, requiring plume and ridge mantle to be compositionally distinct, and this distinction to be time-integrated (Stracke & Béguelin, 2024; Stracke et al., 2005, 2022; Zindler & Hart, 1986). These chemical observations indicate that density gradients in the mantle are both thermal and compositional in origin.

The density of a parcel of mantle is a key parameter of mantle convection, as it controls vertical fluxes through the buoyant force (Westaway, 1993). In turn, mantle convection results in local density changes through cooling, melt-extraction and crustal recycling at the crust-mantle boundary (Afonso & Schutt, 2012; Ishii et al., 2019; Ricolleau et al., 2010). This feedback loop between the cause of mantle convection and its own effects is a critical feature of the Earth system, as it governs the thermochemical budget of our planet. Both geodynamical and geochemical models of mantle evolution hinge on estimating the magnitude of thermochemical processing through time when addressing a wide range of research questions such as the extent and timing of continental crust extraction, the origin of water and other volatiles at the surface, and Earth's early composition and processes (Bolfan-Casanova, 2005; Cawood & Hawkesworth, 2019; Hirschmann & Kohlstedt, 2012; Kumari et al., 2016, 2019; Ohtani, 2005; Peslier et al., 2017; Walzer & Hendel, 2022; Walter & Trønnes, 2004). The generalization of these models to terrestrial planets is also useful for exoplanet characterization (Dorn et al., 2015; Guimond et al., 2024; Noack & Breuer, 2014; Putirka, 2024).

Because the mantle is inaccessible for direct observation, the parameter space of mantle convection remains relatively open. Models are limited by the lack of constraints on key parameters such as the temperature of the core-mantle boundary, the viscosity profile of the mantle, the buoyancy number of recycled crust, and the gradients in composition between the lower and upper mantle (Frost et al., 2022; Kaufmann & Lambeck, 2000; Rudolph et al., 2020; Wang et al., 2020). These compositional gradients are of particular interest, however, as they can link two fundamentally different classes of models: forward geodynamical mantle circulation models and geochemical inversion models of MORB and OIB radiogenic isotope data.

1.2. Linking the Parameter Space of Geodynamical and Geochemical Models

Mantle source composition is the sum of two main processes: melt extraction and crustal recycling. Melt extraction through partial melting causes peridotite to become more chemically depleted in heavy major elements such as Fe and Si, thus lowering its density (Afonso & Schutt, 2012). It also causes a steep chemical depletion in both radioactive and radiogenic trace elements (Rb, Sr, Sm, Nd, Lu, Hf, U, Th, Pb) (Salters & Stracke, 2004; Stracke & Béguelin, 2024; Stracke & Bourdon, 2009). Crustal recycling into the mantle at subduction zones adds dense mafic material to peridotite (high Fe and Si contents) along with a cargo of radioactive and radiogenic trace elements (Ishii et al., 2019; Ricolleau et al., 2010; Sun & McDonough, 1989). The local magnitude of melt extraction (= melt depletion) and crustal recycling are quantitative parameters of both geodynamical and geochemical models. In geodynamical models, compositional density affects vertical fluxes through the buoyant force (Mulyukova et al., 2015; Panton et al., 2023). In isotope modeling (geochemical inversions), peridotite melt depletion and crustal recycling are directly linked to parent/daughter ratios and elemental concentrations through solid/melt partition coefficients (oceanic crust forms through melt aggregation) (Stracke & Bourdon, 2009).

A quantification of the extent of peridotite depletion and of the amount of crustal recycling can be extracted from the results of both classes of models at the local scale: for a parcel of mantle in geodynamical models and for a given sample in geochemical inversions. The absolute values for these two parameters locally at the end of a full-mantle geodynamical model run or corresponding to the multi-isotope composition of a given sample in inverse geochemical modeling are a function of the local and global values of all other model parameters. In geodynamical models, these include viscosity profiles, core-mantle thermal parametrization, and the buoyancy number of recycled crust (Barry et al., 2017; Bower et al., 2013; Bunge et al., 1998, 2002; Davies et al., 2012; Flament et al., 2022; Panton et al., 2025). In geochemical models, these include solid/melt partition coefficients, the ages of processes, oceanic crust alteration, sediment addition, and dehydration (Béguelin, Stracke, et al., 2025; Stracke et al., 2003).

In the present study, we compare the compositional results of runs from a forward geodynamical mantle circulation model (Baumgardner, 1985; Panton et al., 2022, 2023; Plimmer et al., 2024) with results from a new geochemical inversion model (presented in Section 2 of this article) that performs an inversion of the global

MORB–OIB radiogenic isotope data set. Our geochemical model is purely chemical and treats samples individually, ignoring the rheological and thermodynamical constraints of mantle circulation. In the geodynamical model, particles circulate within a 3D mantle grid. Circulation, melting and incorporation of crustal material is governed by known or assumed rheological and thermodynamical parameters but without any control over melt chemistry (Bunge et al., 2002; van Heck et al., 2016).

Rather than comparing the absolute results of peridotite depletion and the amount of crustal recycling in the two classes of models, we compare the relative difference between these results in the plume mantle (sampled by OIB) and in the upper mantle sampled by MORB. This difference corresponds to the main vertical compositional gradient in the mantle and directly scales with the compositional buoyancy of upwelling plumes, regardless of absolute values. We investigate whether the mean relative plume—ridge differences for peridotite depletion and the amount of recycled crust in any given geodynamical model run corresponds to its counterpart in a run of our geochemical inversion model (all MORB and OIB). If the results match, the two parameter spaces of other geochemical and geodynamical model variables can be simultaneously reduced.

1.3. The Need for a Quantitative Approach to MORB–OIB Geochemical Data Interpretation

In the geodynamical model, the amount of recycled crustal material and the extent of peridotite depletion can be directly extracted from the particles situated right under the melting zones of hotspots and ridges at time = present day. In contrast, these two parameters cannot be directly extracted from geochemical isotopic data and instead need to be constrained in a mantle source evolution model taking into account a number of equally important parameters such as the timing of source modification and the surface processes affecting the composition of recycled crustal material (sediments addition, alteration, dehydration). Due to the complexity of this geochemical problem, most geochemical studies of global OIB and/or MORB radiogenic isotope data instead focus on the distribution of the data set itself. The overwhelming angle of study in the field is that of isotopic endmembers bounding the data cloud, which are by extension thought of as mantle components (e.g., the DMM, EM, HIMU, FOZO, PREMA components and the DUPAL signature) (e.g., Cai et al., 2023; Hofmann, 1997; Weis et al., 2023). This qualitative approach is problematic as peridotite and recycled crustal materials have vastly different incompatible element concentrations (i.e., Sr, Nd, Hf, Pb budgets) and melt productivities, causing melting and mixing processes to obscure the signal of the actual source endmembers (Basch et al., 2025; Rudge et al., 2013; Stracke, 2021; Stracke & Béguelin, 2024).

Quantitative radiogenic isotope models of mantle source evolution focused on the composition of individual samples are quite rare (Béguelin, Stracke, et al., 2025; Stracke et al., 2003), with most quantitative studies only attempting to explain the slope of a linear regression through the global multi-isotope data set (the mantle or terrestrial array: Chauvel et al., 2008; Israel et al., 2020; Jones et al., 2019; Panton et al., 2022; Willig & Stracke, 2019; Willig et al., 2020). In the present study, we use a quantitative mantle source model (our geochemical inversion model), calculating the effects of chemical modifications through geological processing from 4.57 Ga to present-day for each of thousands of samples from a global OIB and MORB compilation of radiogenic isotope data (described below in Section 2). This approach allows deriving the crustal recycling and peridotite depletion parameters necessary for a comparison with the geodynamical model results.

2. Description of the Geochemical Inversion Model

2.1. General Approach

We use a *Monte Carlo* model to calculate the radiogenic isotope signatures of random model melts generated through depletion, recycling, and aging in a mantle source model. The isotope signature of each random model melt is then compared to the natural MORB–OIB data set. The model parameters leading to *Monte Carlo* simulations that successfully match natural data are logged, allowing to examine the parameter space yielding real individual samples. The modeling is performed in *Python* language (version 3.9.13), making use of the *NumPy* package (version 1.21.5) (Harris et al., 2020). The array-based calculations enabled by this package allow running $5 \cdot 10^5$ full simulations per second ($= 5 \cdot 10^5$ different model melts) on a 2021 *MacBook Pro* (single-threaded calculations). $2 \cdot 10^{10}$ simulations can be run overnight. The *pandas* package (version 1.4.4) (McKinney, 2011) and the *Matplotlib* package (version 3.5.2) (Hunter, 2007) were used to generate tables and figures.

Table 1
Model Parameters Description and Input Ranges

Parameter	Description	Range min	Range max
Parameters for the peridotite			
$X_{DM,Per}$	Proportion of the PM being depleted prior to re-homogenization	0.0	1.0
$F_{DM,Per}$	Degree of melting of the proportion of PM being depleted	0.0	0.1
$t_{DM,Per}$	Age of PM depletion and re-homogenization	2.5 Ga	4.0 Ga
F_{dPer}	Degree of peridotite melt-depletion (= second depletion event)	0.0	0.1
t_{dPer}	Age of melt-depletion (= second depletion event)	500 Ma	2.5 Ga
F_{Per}	Melting degree of peridotite during present-day magmatism	0.02	0.15
F_d	Total degree of peridotite melt-depletion: $F_d = X_{DM,Per} \cdot F_{DM,Per} + F_{dPer} \cdot (1–X_{DM,Per} \cdot F_{DM,Per})$	(calculated from other inputs)	
Parameters for the recycled mafic crust			
$X_{DM,MC}$	Proportion of the PM being depleted prior to re-homogenization	0.0	1.0
$F_{DM,MC}$	Degree of melting of the proportion of PM being depleted	0.0	0.1
$t_{DM,MC}$	Age of PM depletion and re-homogenization	2.5 Ga	4.0 Ga
F_{MC}	Degree of melting leading to the mafic crust to be recycled	0.01	0.1
f_{Alt}	Extent of mafic crust alteration	0.0	1.0
Parameters for the recycled sediments			
t_{CC}	Age of the continental crust	2.5 Ga	4.0 Ga
Parameters for the recycled mafic crust + sediments (= recycled crust)			
t_{RC}	Age of the recycled crust	500 Ma	2.5 Ga
f_{Sed}	Mass proportion of sediments in recycled crust	0.0	0.1
f_{Dhy}	Extent of dehydration of the recycled mafic crust and sediments	0.0	1.0
f_{RC}	Mass fraction of recycled crust in modeled mantle source	0.00	0.15
F_{RC}	Melting degree of recycled crust during present-day magmatism	Fixed at 0.65	

The modeled chains of events, natural data and matching criteria are discussed below, while the elemental partitioning, isotopic growth, and the statistical treatment of successful simulations are discussed in the Text S1 of Supporting Information S1. Note that while the geochemical model contains 18 input parameters (Table 1), only the amount of recycled crust in the source f_{RC} and the extent of peridotite depletion F_d are used in our cross-model comparison with the geodynamical model and subsequent discussion.

2.2. Modeled Chains of Events

Each individual model simulation corresponds to an entirely distinct mantle source with a composition and history entirely independent from that of other simulations. While simulations are quantitatively distinct from each other, they all follow an identical qualitative scenario that describes the chemical depletion of mantle peridotite by melt extraction, the recycling of subduction-modified oceanic crust and sediments, radiogenic isotope growth, and the fractional melting of this heterogeneous source leading to a model oceanic basalt from 4.57 Ga to today. In each simulation, two peridotite depletion events and one crustal recycling event are modeled. Three components are modified, aged and mixed: Peridotite, mafic crust, and sediments. The sequence of component-modifying and mixing events is detailed in Figure 1, parameter descriptions and ranges are listed in Table 1, and model constants are detailed in Tables S1 and S2 of Supporting Information S1.

Both mafic crust and peridotite are derived from the primitive mantle (PM) of Sun and McDonough (1989) (Table S1 in Supporting Information S1) after its depletion into a model depleted mantle (model DM). This depletion is modeled as follows: a proportion X_{DM} of the PM is depleted with a degree of melting F_{DM} at time t_{DM}, followed by a re-homogenization of the untouched PM with the restite (re-homogenized source = $(1–X_{DM}) \cdot$ PM + $X_{DM} \cdot$ restite) (see Table 1 for ranges). The reason for this re-homogenization is to keep

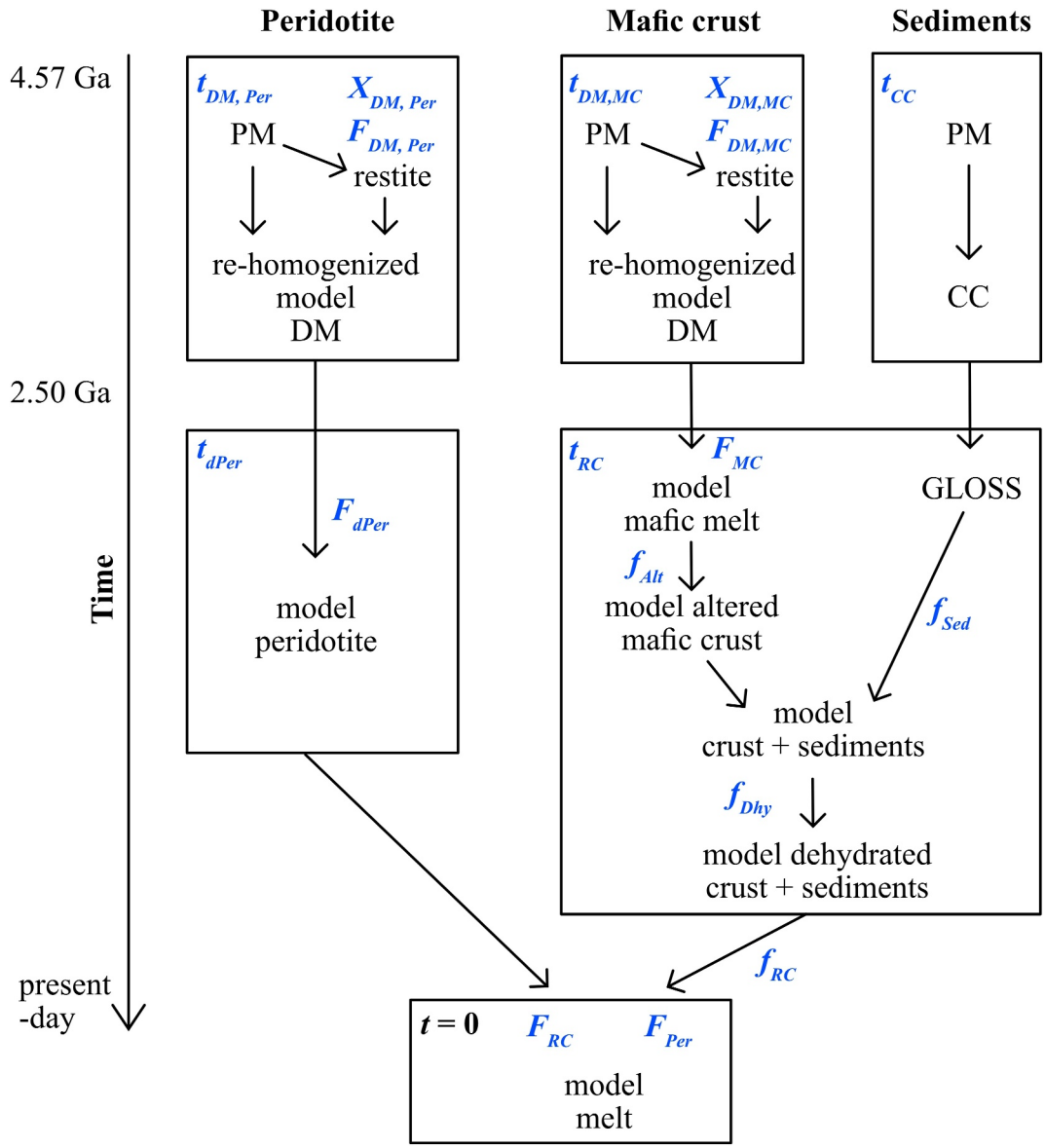

Figure 1. Diagram of the model's logic. This sequence of events is repeated in each simulation with different numerical values for the parameters in blue. Parameter description and ranges are in Table 1. PM, CC, GLOSS compositions, alteration factors, dehydration factors, and melt *Kd* factors are treated as constants and listed in Table S1 of Supporting Information S1. PM, Primitive mantle (Sun & McDonough, 1989); CC, Continental crust (Rudnick & Gao, 2003); GLOSS, Global subducting sediment (Plank & Langmuir, 1998). DM, Depleted mantle (composition calculated in the model in each simulation).

incompatible elements in the mantle source, leading to a depleted but not refractory mantle. Because this re-homogenization occurs in a closed system, its timing has no bearing on the model. It is however set to occur before subsequent model events. $X_{DM,Per}$, $F_{DM,\ Per}$, $t_{DM,Per}$ denote the three variables quantifying the formation of the model DM in the chain of events leading to peridotite, while $X_{DM,MC}$, $F_{DM,MC}$, $t_{DM,MC}$ denote these for the chain of events leading to the mantle source of mafic crust. In our model setup, X_{DM} therefore quantifies how primitive the mantle source remains, with low X_{DM} values corresponding to a low mass proportion of the source affected by depletion, and thus to a more primitive source.

This depletion of the PM to yield a model DM is treated individually for each model simulation and between the mafic crust and peridotite chains of events (Figure 1). Mantle evolution is therefore treated locally rather than globally in the model, contrasting with more classic approaches to mantle geochemical modeling (Chauvel

et al., 2008; Salters & Stracke, 2004; Stracke et al., 2003; Willig et al., 2020; Workman & Hart, 2005). We did however run a number of model variants where $X_{DM,MC} = X_{DM,Per}$, $F_{DM,MC} = F_{DM,Per}$, and $t_{DM,MC} = t_{DM,Per}$ for each individual simulation, reflecting a scenario where recycled mafic crust and underlying mantle lithosphere (=peridotite) remain together during mantle convection.

At a time $t_{d\text{Per}}$, a second peridotite depletion event is modeled, yielding model peridotite from its precursor model DM with a melting degree $F_{d\text{Per}}$ (see the peridotite chain of events in Figure 1). This modeled event allows testing the relatively recent paradigm stating that peridotite more depleted than the classical DM of Salters and Stracke (2004) and Workman and Hart (2005) is present in the source of oceanic basalts and affects their multi-isotope systematics (Béguelin et al., 2019, 2025a; Bizimis et al., 2007; Byerly & Lassiter, 2014; Ferrando et al., 2024; Salters et al., 2006; Sanfilippo et al., 2019, 2024, 2025; Sani et al., 2020, 2024; Stracke & Béguelin, 2024; Stracke et al., 2019). As always, $t_{d\text{Per}}$ and $F_{d\text{Per}}$ take individual values in each simulation within the ranges of Table 1. In this second depletion event, either no depletion occurs ($F_{d\text{Per}} = 0$) or all the local peridotitic source sees some partial melting, as there is no "X_d" parameter (thus equivalent to "X_d" = 1 in all cases). The combined magnitude of the two depletion events affecting peridotite is described by the parameter F_d with

$$F_d = X_{DM,Per} \cdot F_{DM,Per} + F_{d\text{Per}} \cdot (1 - X_{DM,Per} \cdot F_{DM,Per})$$

$1 - X_{DM,Per} \cdot F_{DM,Per}$ is a mass-balance factor used to correct $F_{d\text{Per}}$ with reference to the starting PM material (the degree of melt-depletion $F_{d\text{Per}}$ is relative to the model DM). F_d is of particular importance as it is used to compare geochemical and geodynamical model results.

Sediments are derived from a continental crust reservoir with the parent/daughter ratios of the average continental crust (CC) of Rudnick and Gao (2003) (Table S1 in Supporting Information S1), splitting from PM at a time t_{CC}. At a time t_{RC}, RC (Recycled Crust = modeled dehydrated crust + sediments) is formed. During this event, sediments acquire the global subducting sediment (GLOSS) composition from Plank and Langmuir (1998) (Table S1 in Supporting Information S1). The mafic crust to be recycled is derived from the corresponding model DM (parametrized by $X_{DM,MC}$, $F_{DM,MC}$, $t_{DM,MC}$: see above for details) with a melting degree F_{MC}, this mafic crust is altered with an extent of alteration f_{Alt} (see detailed alteration budget B_{Alt} in Table S1 of Supporting Information S1), altered mafic crust and sediments are mixed with a mass proportion of sediments f_{Sed}, and this mixture is dehydrated with an extent of dehydration f_{Dhy} (see detailed dehydration mass loss ratios R_{Dhy} in Table S1 of Supporting Information S1) (these alteration and mixing events all happen at time t_{RC}). This segment of the model is similar to the quantitative crust recycling model presented by Stracke et al. (2003); however, again, t_{CC}, t_{RC}, F_{MC}, f_{Alt}, f_{Sed}, and f_{Dhy} take different random values in each individual simulation within the ranges listed in Table 1, and we do not use the composition of today's MORB as a proxy for that of recycled mafic crust. This is because our model is used to interpret the isotopic signature of individual MORB (along with that of OIB), which would lead to circular reasoning.

At $t = 0$ (present day), recycled crust mixes with model peridotite (solid—solid mixing) with a mass proportion of crust f_{RC}. f_{RC} is of particular importance as it is used to compare geochemical and geodynamical model results. Recycled crust and peridotite melt individually with melting degrees F_{RC} and F_{Per} before the aggregation and eruption of these melts (mixing proportion = f_{RC} corrected for F_{RC} and F_{Per}). f_{RC} and F_{Per} take individual values in each simulation, while F_{RC} is 0.65 (=65%) in all simulations to avoid redundancy with f_{RC} variability: for the large degrees of melting consistent with mafic lithologies in the mantle (e.g., $F > 0.2$, Brunelli et al., 2018), the melting degree and relative abundance of recycled crust in the heterogeneous mantle source have near-identical effects on the elemental concentrations and isotope composition of aggregated melts.

2.3. Natural Data and Model Matching Criteria

The isotope data set used in the model comprises 1031 MORB and 1615 OIB samples (Figure 2). MORB were compiled from PetDB in August 2023 (with *Tectonic Setting* = *SPREADING_CENTER*). OIB were compiled from GEOROC in February 2024 (*Location* = *Oceanic Island Groups*). Data and references can be found in Tables S3 and S4. The geographical distribution of samples is shown in Figure S1 of Supporting Information S1. All samples in this data set have measured values for $^{87}Sr/^{87}Sr$, $^{143}Nd/^{144}Nd$, $^{176}Hf/^{177}Hf$, $^{206}Pb/^{204}Pb$, $^{207}Pb/^{204}Pb$, and $^{208}Pb/^{204}Pb$ radiogenic isotope ratios. To allow an efficient comparison of model isotope signatures with natural data, we map the full natural data set in a 6-dimensional Boolean array with a resolution of

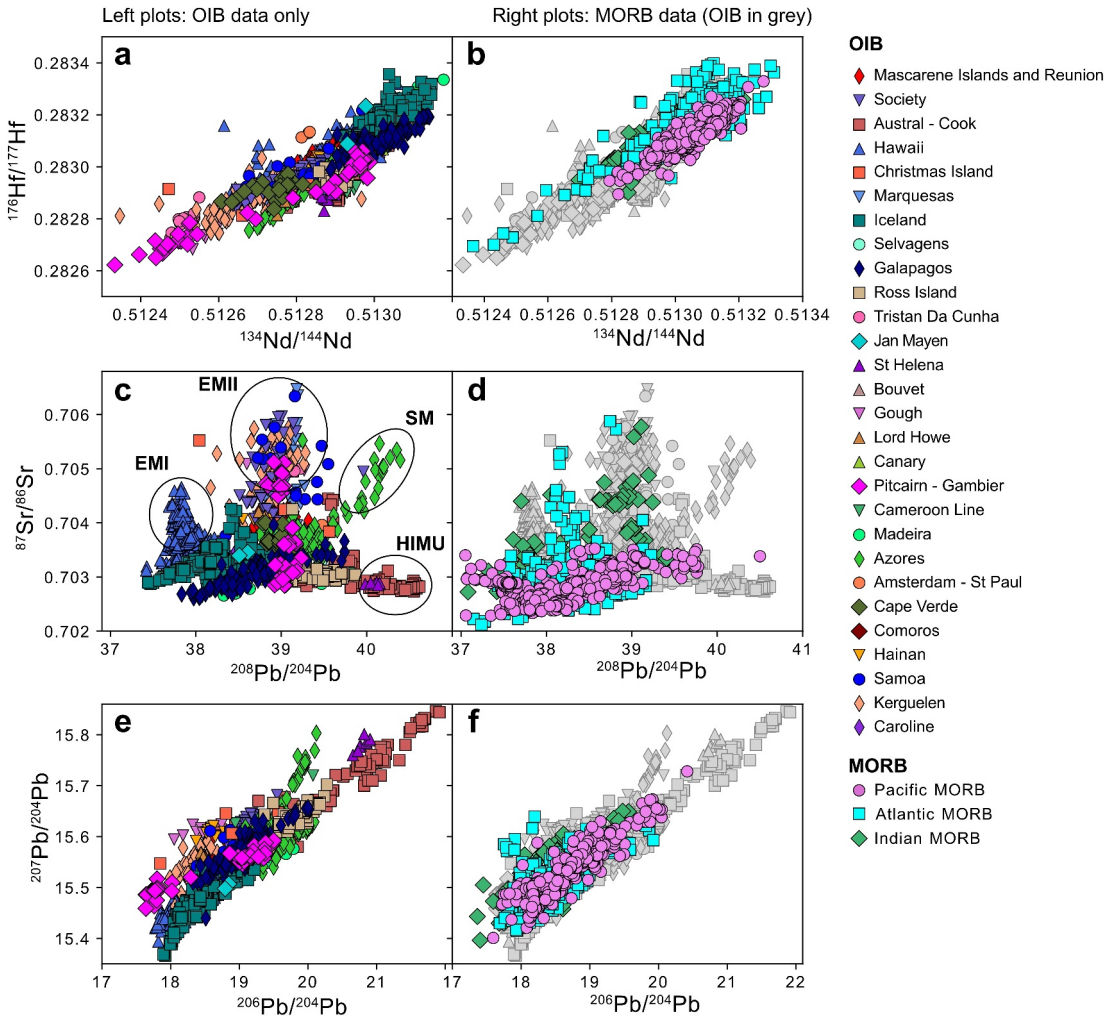

Figure 2. Multi-isotope plots of the natural data used in the model. (a, b) $^{143}Nd/^{144}Nd$–$^{176}Hf/^{177}Hf$; (c, d) $^{208}Pb/^{204}Pb$–$^{87}Sr/^{86}Sr$; (e, f) $^{206}Pb/^{204}Pb$–$^{207}Pb/^{204}Pb$. Left-hand plots show only OIB data. Right-hand plots show MORB data with OIB data grayed-out. Fields in c identify samples with affinities to traditional mantle isotopic endmembers. SM, São Miguel (Azores).

1/30 of the data set range for each of the 6 isotope ratios. Any Sr–Nd–Hf–Pb–Pb–Pb isotope composition R within the range of natural data can be translated to an index (i_0, i_1, i_2, i_3, i_4, i_5) of this array through the following equation (where i_j is an integer):

$$i_j = \left(R_j - R_{j_{\min}}\right) \cdot\ 30\ /\ \left(R_{j_{\max}} - R_{j_{\min}}\right)$$

where $j = \{0: {}^{87}Sr/^{87}Sr, 1: {}^{143}Nd/^{144}Nd, 2: {}^{176}Hf/^{177}Hf, 3: {}^{206}Pb/^{204}Pb, 4: {}^{207}Pb/^{204}Pb, 5: {}^{208}Pb/^{204}Pb\}$, $R_{j\min}$ and $R_{j\ \max}$ = minimum and maximum isotope composition of the natural data set for an isotope ratio j (Table S2 in Supporting Information S1).

1,906 elements (or cells) of this array include natural samples with an average of 1.4 samples in each of these 1,906 cells. This 6-dimensional array is sparse as only 0.00026% of its elements include natural samples (total of 30^6 total cells in the array). If a simulated model isotope composition falls in a cell occupied by one or several natural samples, the simulation is considered valid and the random *Monte Carlo* parameters leading to it are logged. For successful simulations, the distance between model isotope composition and that of any natural sample in the same cell is on average 1/3 of the model resolution shown in Table S2 of Supporting Information S1. In addition, simulations are rejected if the elemental concentrations of the model final melt are significantly higher than those of natural mantle melts, that is Sr > 1,267 μg/g, Nd > 78 μg/g, Hf > 11 μg/g, and Pb > 8.5 μg/g.

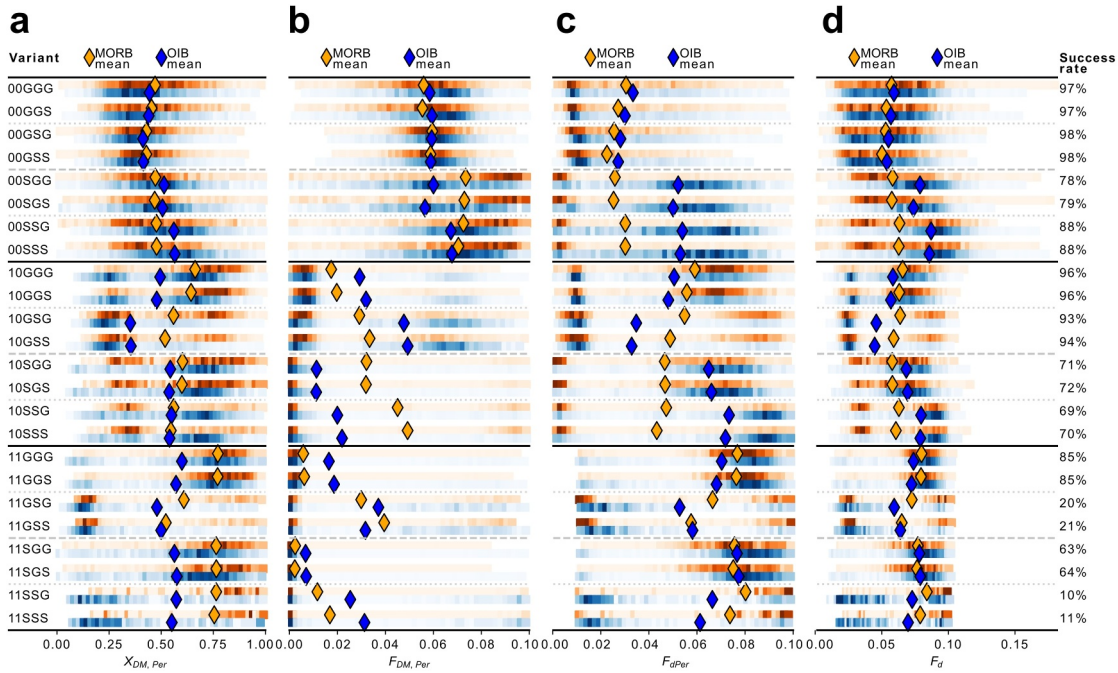

Figure 3. Peridotite melt-depletion results for all variants of the geochemical model. Variants are listed on the left and their success rate on the right (= percentage of data cells with one or more matching simulation). Color saturation represents the relative distribution of results for each variant, for MORB in orange and for OIB in blue. Diamonds show means, weighted for plume buoyancy for OIB. (a) $X_{DM,Per}$: Proportion of the *PM* source being affected by melt-depletion (prior to 2.5 Ga). (b) $F_{DM,Per}$: Degree of melt-depletion of the *PM* fraction affected by melt-depletion (prior to 2.5 Ga). (c) F_{dPer}: Degree of melt-depletion of the *PM* + *melt-depleted* re-homogenized source (after 2.5 Ga). (d) F_d: Total degree of melt-depletion.

3. Results and Discussion of the Geochemical Inversion Model

3.1. Model Variants and Success Rates

We run the 24 model variants listed in Figure 3. For ease of identification, variant names encode their distinctive input characteristics. Variants differ by whether the model DM of mafic crust and that of peridotite in a given simulation are identical (if the proportion, melting degree and age of DM formation ($X_{DM,Per}$, $F_{DM,Per}$, $t_{DM,Per}$) = ($X_{DM,MC}$, $F_{DM,MC}$, $t_{DM,MC}$)). This characteristic corresponds to the first character of names with 0 for distinct and 1 for identical. The second variant characteristic is whether mafic crust formation corresponds in timing and melting degree to the second peridotite depletion event (F_{dPer}, t_{dPer}) = (F_{MC}, t_{RC}). This is encoded with the second character of names with 0 for independent and 1 for corresponding. Model variants also differ by whether peridotite melting events (of melting degree $F_{DM,Per}$, $F_{DM,MC}$, F_{dPer}, F_{MC}, F_{Per}) occur in the garnet or spinel stability field. The third character of variant names denotes the stability field for the DM forming events (G = garnet, S = spinel), the fourth character denotes the field for mafic crust formation and the second peridotite depletion event (of magnitudes F_{MC} and F_{dPer}), and the fifth character denotes the field for the present-day melting of peridotite. Model variants are to be thought of as simplified endmember-type scenarios in our exploration, likely bounding Earth mantle's true complexity.

We run $2 \cdot 10^{10}$ *Monte Carlo* simulations per model variant. Model variants where DM formation occurs in the garnet stability field (xxGxx) show much higher rates of success than the spinel case (Figure 3). The second-order control on the success rate is whether peridotite and mafic crust DM formation are tied or not, with the untied case (0xxxx) showing higher rates of success. Variants where mafic crust formation corresponds to the second peridotite depletion event (names starting with 11) show the lowest rates of success. Table S5 is a spreadsheet containing the detailed model results for individual ocean basins (MORB) and plumes (OIB). 8 model variants show overall success rates of >94% (i.e., >94% of isotope data cells can be modeled). In these variants, only the Pitcairn-Gambier and Gough plumes (with EMII-type characteristics, Weis et al., 2023) pose a significant challenge (= partial results for these plumes). 12 variants show 64%–88% success rates with the Madeira, St.

Helena and Austral-Cook plumes (with HIMU-type characteristics) posing additional challenges. 4 variants show rates of success <22% with most groups being challenging to model.

Peridotite depletion, mafic crust recycling and non-magmatic processes are detailed below, while the present-day melting and trace element ratios are discussed in the Text S2 and Figures S2–S5 of Supporting Information S1.

3.2. Time-Integrated Peridotite Depletion

In variants 0xxxx, the depleted mantle yielding the peridotitic fraction of the mantle source is calculated with the parameters $X_{DM,Per}$, $F_{DM,Per}$, $t_{DM,Per}$, and the depleted mantle yielding the source of the mafic crust is calculated with the parameters $X_{DM,MC}$, $F_{DM,MC}$, $t_{DM,MC}$ (Figure 3, Figures S6 and S7 in Supporting Information S1). As a reminder, X_{DM} is the mass fraction of the source affected by depletion, F_{DM} is the degree of partial melting this fraction experiences, and t_{DM} is the depletion age. This initial mantle depletion event is modeled to take place prior to 2.5 Ga.

In variants 0xxxx, $X_{DM,Per}$ show similar values compared to $X_{DM,MC}$ (Figure S6 in Supporting Information S1), however $F_{DM,Per}$ values are higher than $F_{DM,MC}$ (0.05–0.10 compared to <0.03), yielding a more depleted DM for the source of peridotite. This difference makes sense conceptually as the mafic material to be recycled in our model is produced by a source devoid of recycled crustal material, unlike modern MORB and OIB. It therefore ought to be more fertile than normal mantle peridotite to resolve this "chicken and egg" situation. In variants 1xxxx ($X_{DM,Per}$, $F_{DM,Per}$, $t_{DM,Per}$) = ($X_{DM,MC}$, $F_{DM,MC}$, $t_{DM,MC}$), this early form of mantle heterogeneity is excluded, leading to lower model success rates (Figure 3).

An important finding of the model is the dependence of peridotite depletion results on the presence or absence of garnet in the melting assemblage during the depletion of the PM to a model DM in the sequence of events leading to mantle source peridotite ($X_{DM,Per}$, $F_{DM,Per}$ parameters at $t_{DM,Per}$ = 4.0 Ga to 2.5 Ga). When garnet is present in the melting assemblage of this early depletion event, $X_{DM,Per}$ and $F_{DM,Per}$ show no clear pattern between MORB and OIB, with means at $X_{DM,Per}$ = 0.4 and $F_{DM,Per}$ = 0.06 (Figure 3). When garnet is absent, however, MORB and OIB results become decoupled with higher $X_{DM,Per}$ values for OIB (= more of the PM affected by depletion) and higher $F_{DM,Per}$ values for MORB (Figure 3).

The splitting of results for the model DM ($X_{DM,Per}$ and $F_{DM,Per}$) between MORB and OIB in the non-garnet case subsequently has a knock-on effect on results of the second peridotite depletion event ($F_{d\mathrm{Per}}$ at $t_{d\mathrm{Per}}$, see Figure 1, Table 1, and Figure S8 in Supporting Information S1). The repartition of $F_{d\mathrm{Per}}$ results (Figure 3) does not depend on the presence of garnet in the melting assemblage of this second depletion event (second letter of model variant names), but is rather fully controlled by the presence of garnet in the melting assemblage of the previous DM-forming event. In the garnet-bearing case, $F_{d\mathrm{Per}}$ values show an identical repartition for MORB and OIB with low F means between 0.02 and 0.03 (Figure 3). In the non-garnet case, however, OIB show depleted $F_{d\mathrm{Per}}$ values with means of 0.05, while MORB show similar means compared to the garnet-bearing case (Figure 3).

To fully assess the extent of time-integrated peridotite depletion, we combine the two consecutive peridotite depletion events into a single metric, the total peridotite depletion F_d (see Section 2.2 for details). Note that F_d does not include the final (third) peridotite melt-depletion event, that is, the present-day generation of MORB and OIB melts, but rather tracks the depletion events affecting the composition and isotope signature of peridotite entering the present-day melting zone.

In variants 00xxx and 10xxx, F_d results show a similar repartition for MORB between the garnet and non-garnet cases (means of 0.06) (Figure 3). OIB F_d results are almost identical to MORB in variants 00Gxx, lower than MORB in variants 10Gxx (means of 0.05), and higher than MORB in variants x0Sxx (means of 0.07). Variants 11xxx show F_d results between 0.06 and 0.09 without a clear MORB-OIB systematic, which is likely a consequence of their low success rate (Figure 3).

Lutetium has a higher solid/liquid partition coefficient *Kd* in the garnet-bearing melting assemblage (Table S1 in Supporting Information S1), leading to a depleted peridotite with a more radiogenic $^{176}Hf/^{177}Hf$ for a given $^{143}Nd/^{144}Nd$ compared to the spinel-bearing case (Salters et al., 2011). The different choices of garnet versus spinel stability field during the successive melt-depletion events modeled across model variants lead to drastically distinct results systematics for F_d in Nd–Hf isotope space (Figure S9 in Supporting Information S1). In most stability field combinations, cells with a radiogenic $^{176}Hf/^{177}Hf$ for a given $^{143}Nd/^{144}Nd$ have higher F_d results

(i.e., the related model melts sample more depleted peridotite). This is the case for xxGGx, xxSGx, and xxSSx combinations (excluding 11SSx and its low success rates). This relation becomes reversed in xxGSx combinations, however, with cells with a radiogenic $^{176}Hf/^{177}Hf$ for a given $^{143}Nd/^{144}Nd$ having lower F_d results.

3.3. Mafic Crust Recycling and Non-Magmatic Processes

As mentioned in Section 2.2, the formation of recycled mafic crust is fully quantified in our model, departing from the traditional approach of using modern MORB as a proxy for mafic crust composition. As a reminder, the depletion of the mantle source of mafic crust is controlled by the variables $X_{DM,MC}$, $F_{DM,MC}$, $t_{DM,MC}$, where $X_{DM,MC}$ is the mass fraction of the source affected by depletion, $F_{DM,MC}$ is the degree of partial melting this fraction experiences, and $t_{DM,MC}$ is the depletion age. Note that the degree of melting of the re-homogenized source leading to mafic crust is denoted by F_{MC} and happens later in the model (post 2.5 Ga).

We find $X_{DM,MC}$ has a strong control on the isotope composition of modern MORB and OIB. This parameter corresponds to how primitive the mantle source of mafic crust is. In all model variants, $X_{DM,MC}$ results span the whole input range, from $X_{DM,MC} = 0$ (= fully primitive mantle) to $X_{DM,MC} = 1$ (= all mantle seeing some melt extraction of degree $F_{DM,MC}$ at time $t_{DM,MC}$), with a mean MORB value of $X_{DM,MC} = 0.75$ and a lower (more primitive) mean OIB value of $X_{DM,MC} = 0.5$. High values of $X_{DM,MC}$ correspond to isotopically depleted cells, while more primitive $X_{DM,MC}$ values (<0.3) correspond to isotopically enriched OIB (EMII-type and São Miguel-type but not EMI-type or HIMU-type) (Figure S10 in Supporting Information S1). This parametrization of the mantle source yielding recycled mafic crust is similar to mantle source models varying the composition of recycled mafic crust from D-MORB to E-MORB (Gale et al., 2013). Béguelin et al. (2017) used such a model to interpret the isotope signature of Eastern Azores with similar results (see also Elliott et al., 2007).

The source of the recycled mafic crust melts with a degree of melting F_{MC} of ~0.05 (see Figure S8 in Supporting Information S1) at time t_{RC}. Mafic crust ages occupy the younger half of the model range (see Table 1 for range) with all t_{RC} means < 1.5 Ga. São Miguel lavas (Eastern Azores) occupy some of the only cells with a significantly old recycled crust age t_{RC} (Figures S10 and S11 in Supporting Information S1). Recycled sediments are derived from a continental crust reservoir (composition in Table 1) of age t_{CC}. The repartition of t_{CC} results across model variants follows that of $t_{DM,MC}$ (garnet vs. spinel control, see above) (see Figure S7 in Supporting Information S1). Sediments are mixed with the mafic crust in a proportion f_{Sed} to form recycled crust, which makes up a proportion f_{RC} of the mantle source of each model simulation. Across all model variants, f_{RC} is the most robust discriminator between MORB and OIB results (Figure 4). f_{RC} values show means of ~0.03 for MORB and ~0.05 for OIB, much lower than the allowed maximum of 0.15. Values higher than 0.05 are found in enriched OIB (EMII-type and São Miguel-type, but not EMI-type and HIMU-type) (Figure 5). The proportion of sediments in the recycled crust f_{Sed} does not vary systematically between MORB and OIB, with only the EMI subset of OIB samples showing values above 0.05 (Figure 5), in agreement with existing geochemical interpretations of this type of isotopic composition (e.g., Blichert-Toft et al., 1999; Eisele et al., 2002). f_{Sed} however shows a clear pattern between variants xxGxx ($f_{Sed} \sim 0.045$) and xxSxx ($f_{Sed} \sim 0.02$), compensating for the effects of garnet versus spinel stability field in Nd–Hf isotope space (Figure 5 and Figure S9 in Supporting Information S1). The systematics of f_{RC} results in the Nd–Hf isotope space is however robust to these parameters (Figure 5).

Alteration of the mafic crust at time t_{RC} is modeled as the addition of Rb and U. Results across model variants show this addition of U is needed to reach natural sample cells with a radiogenic $^{206}Pb/^{204}Pb$ for a given $^{207}Pb/^{204}Pb$ (Figure 5). The subsequent dehydration of the mafic crust + sediments mixture (also at t_{RC}) is needed to explain OIB samples with the most radiogenic Pb (São Miguel-type and HIMU-type) (Figure 5). Modeled extents of alteration f_{Alt} and dehydration f_{Dhy} both occupy their whole input range (Figure 4).

3.4. OIB—MORB Relative F_d and f_{RC} Results

The extent of peridotite depletion F_d and the amount of recycled crust f_{RC} are also parameters tracked in the geodynamical model. The F_d and f_{RC} results for MORB and OIB in the geochemical inversion model can therefore be compared with those of plumes and ridges in geodynamical model runs. However, in the geodynamical model, the absolute F_d and f_{RC} values are dependent on the starting compositional mixture used (see Text S3 in Supporting Information S1). We therefore calculate and discuss the relative offsets between mean OIB and MORB values:

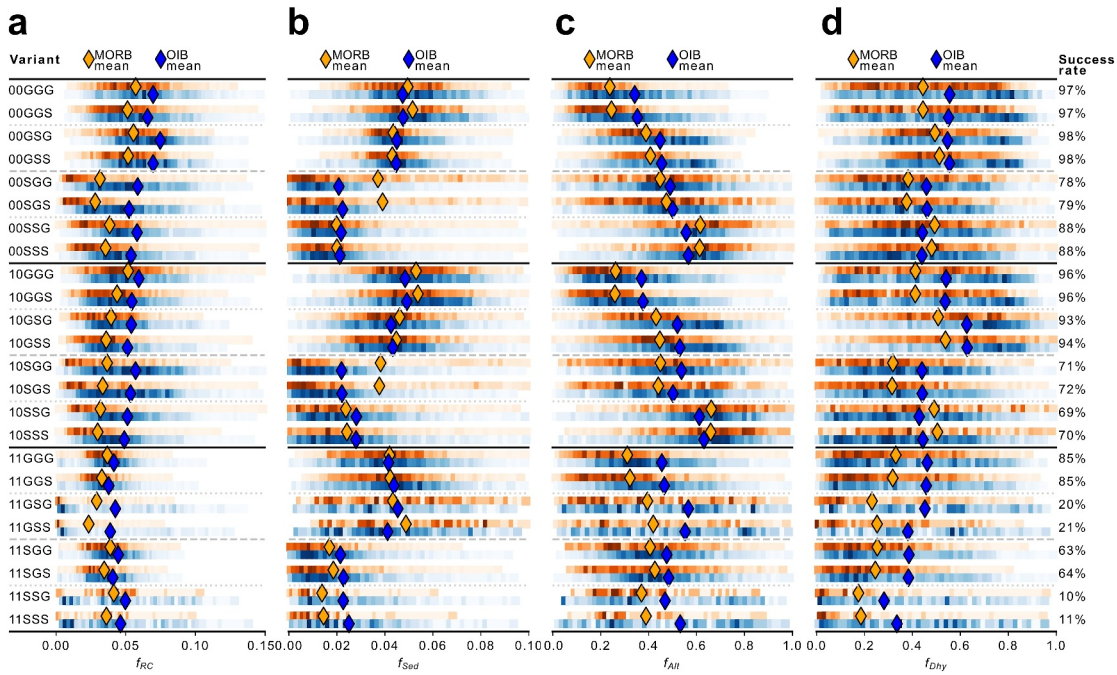

Figure 4. Mafic crust recycling and non-magmatic processes results for all variants of the geochemical model. Variants are listed on the left and their success rate on the right (= percentage of data cells with one or more matching simulation). Color saturation represents the relative distribution of results for each variant, for MORB in orange and for OIB in blue. Diamonds show means, weighted for plume buoyancy for OIB. (a) f_{RC}: Mass fraction of recycled crust in modeled mantle source. (b) f_{Sed}: Mass proportion of sediments in recycled crust. (c) f_{Alt}: Extent of mafic crust alteration. (d) f_{Dhy}: Extent of dehydration of the recycled mafic crust and sediments.

$$\Delta F_d = F_d^{\mathrm{OIB}} - F_d^{\mathrm{MORB}}$$

$$\Delta f_{\mathrm{RC}} = f_{\mathrm{RC}}^{\mathrm{OIB}} - f_{\mathrm{RC}}^{\mathrm{MORB}}$$

Values for ΔF_d range between −0.018 and +0.024 across model variants, reflecting the mean OIB F_d variations described above. Δf_{RC} values are always positive, ranging from +0.005 to +0.027 (Figure 6).

In order to integrate all the results of the geochemical inversion model, we calculate the unique inter-variant means $\Delta F_d^{\mathrm{Geochem}}$ and $\Delta f_{\mathrm{RC}}^{\mathrm{Geochem}}$. These means are weighted at the success rate of each variant, yielding $\Delta F_d^{\mathrm{Geochem}} = +0.004 \pm 0.012$ and $\Delta f_{\mathrm{RC}}^{\mathrm{Geochem}} = +0.015 \pm 0.006$.

3.5. Self-Consistency of the Geochemical Inversion Model and Validity of Assumptions

Our mantle melting parametrization is simple, using bulk melt/rock partition coefficients for peridotite and recycled crust rather than a detailed thermodynamical calculation of melting assemblages. However, we keep peridotite melting degrees as free parameters (for past and present-day melting) and explore the consequences of melting in the garnet versus spinel stability field at various periods of mantle differentiation using model variants as endmember scenarios (see details in Figure 6). This approach allows assessing the sensitivity of model results to variable melting scenarios, a contextualization that a more deterministic model would obscure.

The geochemical model treats each sample separately, effectively considering a unique mantle for each sample. This means that our model does not consider the binary mixing of melts from two heterogeneous mantle sources as a potential process to explain isotope data at the local scale. We test whether our model results are equivalent to a binary melt mixing scenario for the lavas from São Miguel, Azores (Groups II and III from Elliott et al., 2007), which are a likely example of such binary mixing (Beier et al., 2007; Béguelin et al., 2017; Elliott et al., 2007). We find our model results for f_{RC}, F_d and t_{RC} change linearly with isotope values along the São Miguel trend, a pattern fully equivalent to the binary mixing of chemically similar melts from two mantle sources with different f_{RC}, F_d, t_{RC} values (Figure S11 in Supporting Information S1).

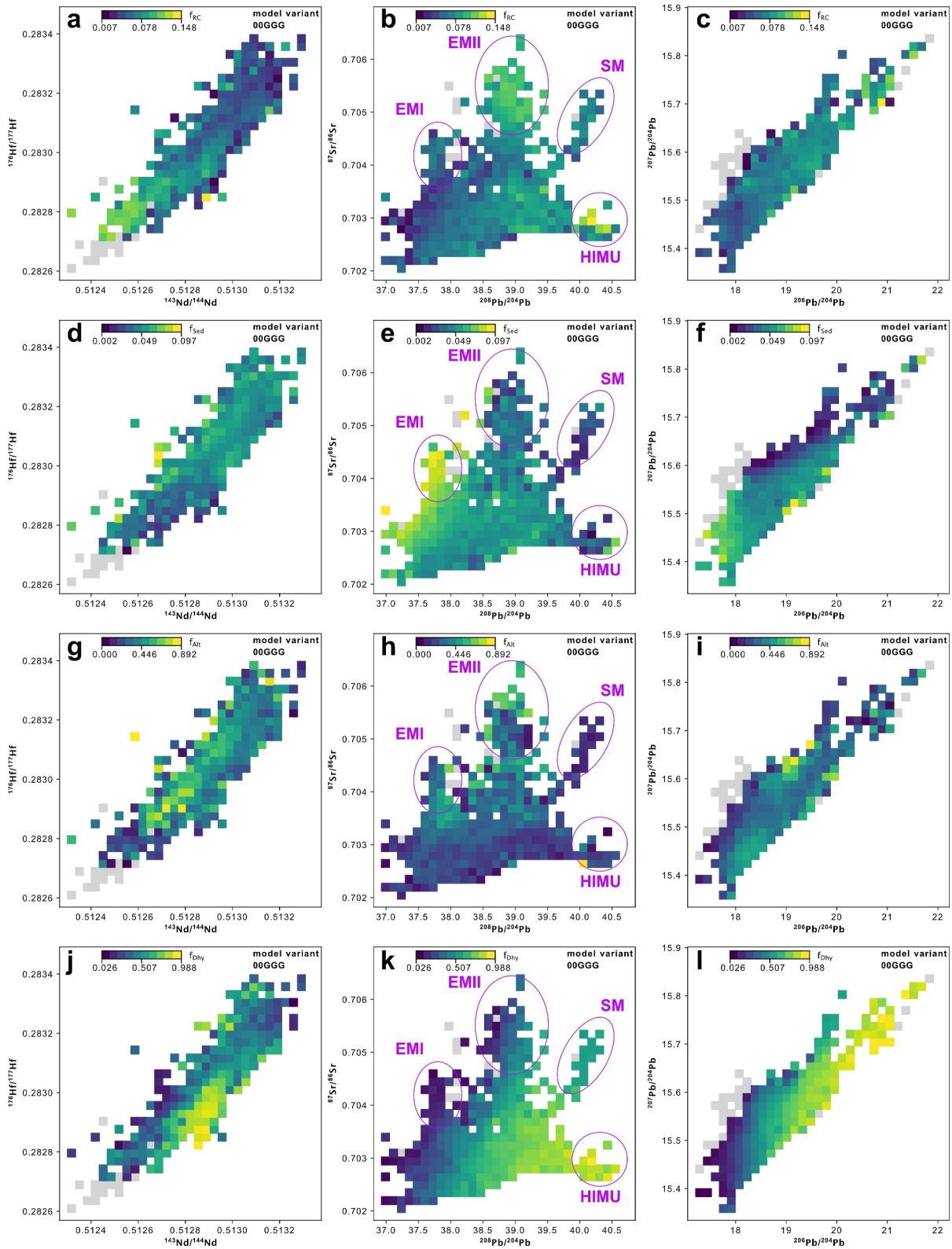

Figure 5. Mafic crust recycling and non-magmatic processes results for variant 00GGG in (left) $^{143}Nd/^{144}Nd$–$^{176}Hf/^{177}Hf$, (center) $^{208}Pb/^{204}Pb$–$^{87}Sr/^{86}Sr$, and (right) $^{206}Pb/^{204}Pb$–$^{207}Pb/^{204}Pb$ space. For (a–c) f_{RC}, (d–f) f_{Sed}, (g–i) f_{Alt}, and (j–l) f_{Dhy} (see Figure 4 caption for spelled-out names). The median results for each modeled cell are plotted. Gray cells have no model results. Fields in (center) highlight cells with affinities to traditional isotopic endmembers. SM, São Miguel (Azores). The Extended Figure 5 Supplement (Supporting Information S2) of this article shows these plots for all 24 model variants.

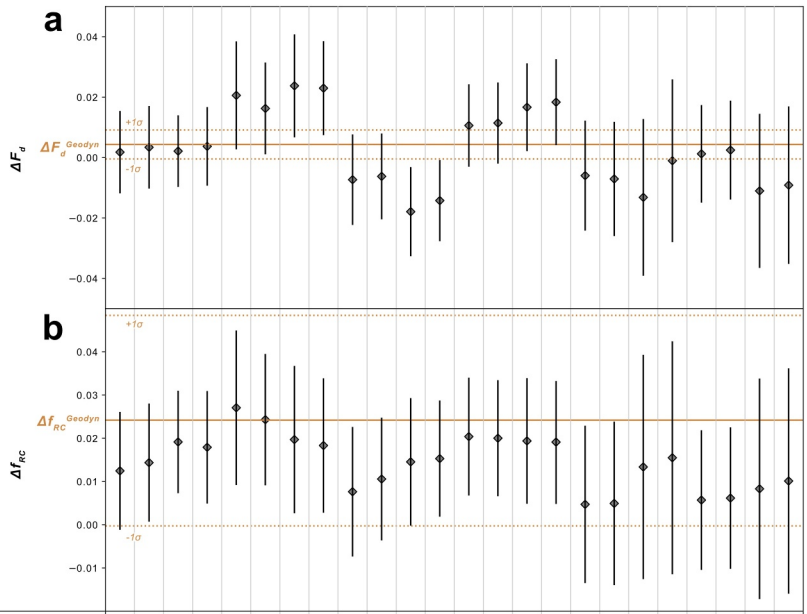

$(X_{DM,Per}, F_{DM,Per}, t_{DM,Per}) = (X_{DM,MC}, F_{DM,MC}, t_{DM,MC})$	no=0, yes=1	0	0	0	0	0	0	0	0	1	1	1	1	1	1	1	1	1	1	1	1	1	1	1
$(F_{dPer}, t_{dPer}) = (F_{MC}, t_{RC})$	no=0, yes=1	0	0	0	0	0	0	0	0	0	0	0	0	0	0	0	0	1	1	1	1	1	1	1
stability field of DM formation	garnet=G, spinel=S	G	G	G	G	S	S	S	S	G	G	G	G	S	S	S	S	G	G	G	G	S	S	S	S
stability field of MC and dPer formation	garnet=G, spinel=S	G	G	S	S	G	G	S	S	G	G	S	S	G	G	S	S	G	G	S	S	G	G	S	S
stability field of present-day melting	garnet=G, spinel=S	G	S	G	S	G	S	G	S	G	S	G	S	G	S	G	S	G	S	G	S	G	S	G	S
model success rate (%)	all data cells	97	98	98	98	79	80	88	88	96	96	94	95	71	72	69	71	86	85	21	22	64	65	11	11
	MORB cells	98	98	99	99	70	71	81	81	97	95	93	93	54	56	59	60	87	88	18	19	50	52	6	6
	OIB cells	97	98	98	98	84	86	93	94	96	97	95	96	82	83	77	78	85	85	21	22	74	75	14	14

Figure 6. Results of geochemical model variants. Variant characteristics and success rates are detailed in the table. (a) Comparison of the geochemical model's ΔF_d values against the mean $\Delta F_d^{\text{Geodyn}}$ value. (b) Comparison of geochemical model's Δf_{RC} values against the mean $\Delta f_{\text{RC}}^{\text{Geodyn}}$ value. Lozenges are individual model variants. Associated bars show the variability among plumes with one standard deviation on each side.

On a global scale, we argue that considering an independent mantle source for each sample is reasonable as only a fraction of the mantle is sampled by today's MORB and OIB. A geochemical model handling Earth's mantle as a whole would need to assume the age and mass of material stored outside the mantle (oceanic and continental crust), of mantle material too depleted to melt (harzburgite, possible "BEAMS": Ballmer et al., 2017), and of enriched material trapped in potential hidden reservoirs untapped by today's oceanic basalts (e.g., Murphy et al., 2010). Making assumptions on the state and composition of the mantle outside the source of each sample would compete with the full-mantle geodynamical model, introducing a form of circular reasoning in the present study. Nonetheless, our model results show that the average age of continental crust formation t_{CC} is similar to the average depleted mantle formation ages $t_{\text{DM,MC}}$ and $t_{\text{DM,Per}}$ in all model variants (Figure S7 in Supporting Information S1).

It is also worth examining whether the timing and extent of post 2.5 Ga peridotite depletion and mafic crust formation are similar. This equivalence is forced by design in model variants 11xxx with ($F_{d\text{Per}}$, $t_{d\text{Per}}$) = (F_{MC}, t_{RC}). In variants 00xxx and 10xxx, the extent of peridotite depletion $F_{d\text{Per}}$ and mafic crust formation F_{MC} are similar, around 5% on average. The ages of these processes however are not, with $t_{d\text{Per}}$ ~1.6 Ga and t_{RC} ~1.0 Ga (Figure S8 in Supporting Information S1). This inconsistency can be explained by the strong control of Pb isotope systematics on the crust recycling age t_{RC}. Pb isotopes have no control on $t_{d\text{Per}}$ due to the low Pb content of peridotite. Average $t_{d\text{Per}}$ values are therefore near the middle of the allowed range (see Table 1), whereas t_{RC} values are young in order to explain samples with a high $^{206}Pb/^{204}Pb$ for a given $^{207}Pb/^{204}Pb$. We argue these inconsistencies do not invalidate our model as (a) parent/daughter ratios and elemental concentrations which are a function of the consistent $F_{d\text{Per}}$ and F_{MC} values have a greater bearing on the isotope composition of aggregated melts than ages, and (b) $t_{d\text{Per}}$ and t_{RC} values are near-identical between MORB and OIB results in any model variant, which means inconsistencies are circumvented when focusing on OIB results relative to MORB as is done in this study instead of focusing on absolute values.

Focusing on the relative ΔF_d and Δf_{RC} values rather than on absolute values further allows circumventing several model assumptions on starting points and on the modeled sequence of events, as these assumptions have an

identical bearing on the OIB and MORB results. These assumptions include starting with a PM composition, modeling only one recycling event, assuming the recycled crust is present as recycled mafic material rather than under the form of a metasomatic cargo (see Herzberg et al., 2014; Niu & O'Hara, 2003), using the GLOSS as the composition of recycled sediments, and correcting the Pb and Th concentration of the PM and CC (see Text S1 in Supporting Information S1).

4. The Forward Geodynamical Mantle Circulation Model

4.1. Model Architecture and Constants

This section presents an overview of the geodynamical model architecture. The associated data, scripts and instructions can be found in the code repository of the present publication (Béguelin, Panton, et al., 2025). The geodynamical model runs presented here were run on the UK national supercomputer Archer 2 as part of the collaborative project MC2—Mantle Circulation Constrained. More details on this project and the geodynamical model can be found in Panton et al. (2022, 2023), Plimmer et al. (2024), and Davies et al. (2025). The numerical geodynamical model models thermochemical convection in a spherical shell representing the mantle by solving the conservation of mass, momentum and energy equations. It does this by solving for the mantle velocity, pressure and temperature on a structured grid (Baumgardner, 1985; Baumgardner & Frederickson, 1985; Bunge & Baumgardner, 1995; Bunge et al., 1995; Stegman et al., 2002; Yang & Baumgardner, 2000). The radial resolution of the grid is 45.2 km, while the lateral resolution varies from 59.9 km at the surface to 32.7 km at the core-mantle boundary (CMB).

The geodynamical model runs discussed here are mantle circulation models, where the surface velocity is prescribed by plate motion history (Müller et al., 2022) going from 1 Ga to present-day. The surface has an isothermal temperature of 300 K, and the CMB is assumed to be a free-slip boundary with an isothermal temperature of 3,800 K in the reference case. Phase transitions at 410 and 660 km depth have Clapeyron slopes of +1.5 (MPa K^{-1}) and −1.0 (MPa K^{-1}), and density changes of 230 (kg m^{-3}) and 380 (kg m^{-3}) respectively. Thermal conductivity is 4 (W m^{-1} K^{-1}), specific heat is 1,100 (J kg^{-1} K^{-1}), thermal expansivity is $1.19 \cdot 10^{-5}$ (K^{-1}) to $3.79 \cdot 10^{-5}$ (K^{-1}), and reference viscosity is $4 \cdot 10^{21}$ (Pa s). The initial condition for the models is produced by first running a mantle convection model, that is, with a free-slip surface boundary condition, until the model approaches a statistical steady-state. Then, the first plate stage velocity boundary condition is applied at the surface for 200 Myr so that the mantle structure relates to the surface velocity boundary condition.

In the geodynamical model, composition is locally tracked on particles which are followed through the flow (van Heck et al., 2016). The bulk composition is described by a single scalar parameter (C), which varies from $C = 0$ (completed depleted) to $C = 0.2$ (average mantle lherzolite), and $C = 1$ enriched (basalt). The composition is mapped from the particles to the grid nodes to incorporate the influence of chemistry on the body force. All geodynamical model runs discussed here are initialized with the following mixture of particles: 40% with $C = 0$, 50% with $C = 0.2$, and 10% with $C = 1$.

To calculate the F_d and f_{RC} values corresponding to MORB and OIB in the geodynamical model, we extract the list of particles present under ridges and plumes active in the model at present-day (see details in Text S3.1 of Supporting Information S1). In each geodynamical model run, F_d and f_{RC} values are calculated from the C values of populations of particles (one F_d and one f_{RC} value per population):

$$F_d = 0.2 - \frac{1}{n-m} \cdot \sum C_i^{\leq 0.2}$$

$$f_{RC} = \frac{\frac{1}{m} \cdot \sum C_i^{>0.2} - 0.2}{0.8} \cdot \frac{m}{n}$$

where n is the total number of particles in a population, and m is the number of these particles with $C > 0.2$, $C_i^{>0.2}$ is the C value of an individual particle with $C > 0.2$, and $C_i^{\leq 0.2}$ is the C value of an individual particle with $C \leq 0.2$.

We then use the same equations as in Section 3.4 to calculate the geodynamical model's $\Delta F_d^{\mathrm{Geodyn}}$ and $\Delta f_{\mathrm{RC}}^{\mathrm{Geodyn}}$. Note that the mean $F_d^{\mathrm{OIB,Geodyn}}$ and $f_{\mathrm{RC}}^{\mathrm{OIB,Geodyn}}$ values are weighted by the calculated buoyancy of each plume recognized in the geodynamical model.

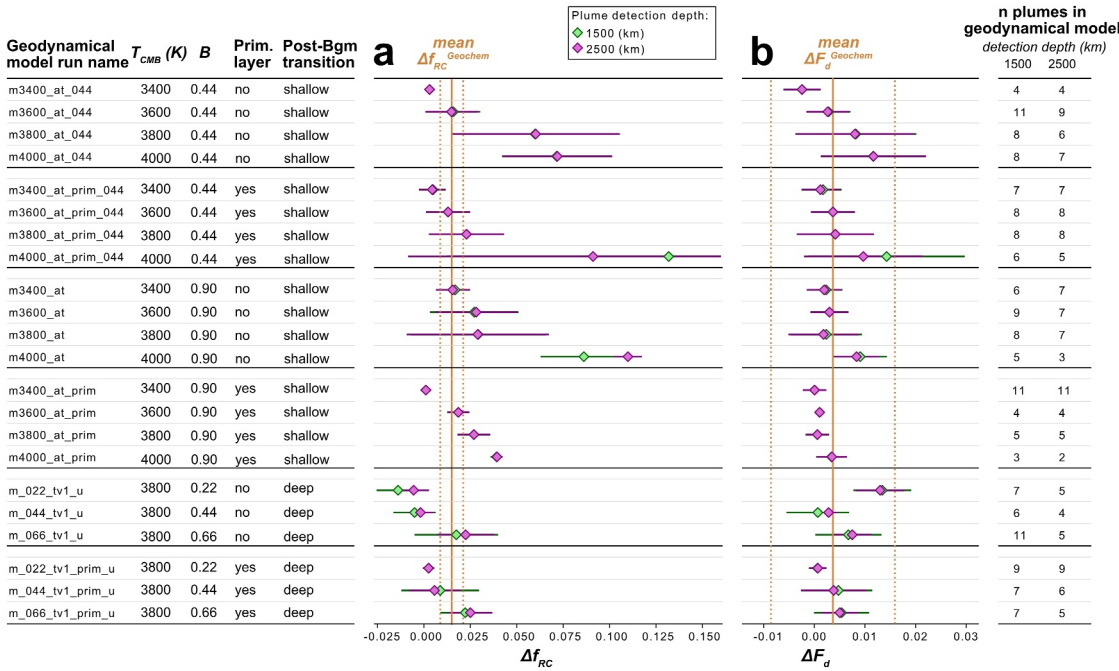

Figure 7. (a) Comparison of geodynamical model Δf_{RC} values against the global $\Delta f_{RC}^{Geochem}$ value (from the geochemical model). (b) Comparison of geodynamical model ΔF_d values against the global $\Delta F_d^{Geochem}$ value (from the geodynamical model). Associated bars show the variability among modeled plumes with one standard deviation on each side. Prim. Layer, primordial layer; Post-Bgm, post-bridgmanite.

Particles are randomly distributed in the mantle until 1 Ga ($\Delta F_d^{Geodyn} = 0$ and $\Delta f_{RC}^{Geodyn} = 0$), after which the geodynamical model starts generating spatial heterogeneities. While the geochemical model is free to generate older MORB-OIB differences, our results show that the well-constrained age of the recycled crust t_{RC} is younger than 1 Ga in most variants (Figure S8 in Supporting Information S1), suggesting that the timeline of MORB-OIB heterogeneity is comparable in the two classes of models.

4.2. Parameter Space of Variables in Geodynamical Model Simulations

The variable parameter space of the geodynamical model explored in the present study include the temperature of the core-mantle boundary (CMB), the buoyancy number of mafic material in the mantle, and the presence or absence of a dense primordial layer at the CMB. An extended parameter space including the mantle viscosity profile and core cooling will be discussed in a related publication centered on the geodynamical model results.

We run geodynamical model simulations with CMB temperatures T_{CMB} of 3,400, 3,600, 3,800, and 4,000 K. Runs with T_{CMB} = 4,200 K proved too unstable to yield accurate results. Mean mantle temperature is adjusted as follows: lower mean temperature for cooler CMB temperatures and higher mean temperatures for hotter CMB temperatures, in an attempt to keep the CMB heat flux similar to the reference case of 3,800 K.

The buoyancy number of mafic material B (dimensionless) in the lowermost mantle is given by the following ratio:

$$B = \frac{\delta\rho_b}{\alpha\rho_0\Delta T}$$

Where $\delta\rho_b$ is the density difference between purely basaltic material and material with an average mantle composition (lherzolite), α is the coefficient of thermal expansivity at the CMB, ρ_0 is the reference density at the CMB, and ΔT is the temperature difference between the CMB and surface boundaries. We run geodynamical model simulations with B values of 0.22, 0.44, 0.66, and 0.90.

Geodynamical model runs are listed in Figure 7. We run a series of geodynamical model simulations varying T_{CMB} at B = 0.44 and B = 0.90, and a series of geodynamical model simulations varying B at T_{CMB} = 3,800 K.

This set of 11 geodynamical model simulations is ran twice: once with a dense primordial layer at the CMB and once without, thus totaling 22 runs. The buoyancy number of the primordial layer is 0.9 in the runs with $B = 0.9$ (Figure 7), and 0.44 in all other runs. More details on primordial layer parametrization are in Panton et al. (2023). Runs focused on T_{CMB} variations have a viscosity profile with a shallow post-bridgmanite transition (2,570 km), whereas runs focused on B have a viscosity profile with a deep transition (2,800 km) (Figure S12 in Supporting Information S1).

5. Integrating the Results From the Geochemical Model and Geodynamical Model Runs

5.1. Geodynamical Model Results and Fit With the Geochemical Model

The geodynamical model runs discussed here produce between 2 and 11 mantle plumes with a mean of 7.2 for a detection depth of 1,500 km, and 6.1 plumes for a detection depth of 2,500 km (Figure 7). In comparison, 48 plumes are identified in the Earth's mantle by Hoggard et al. (2020), with 33 of these plumes accounting for 95% of the total buoyancy flux. According to these authors, the 8 strongest plumes on Earth account for 45% of this total (Iceland, Afar, Hawaii, Cape Verde, Samoa, Balleny, Reunion, and Galapagos). The cumulative sum of the total buoyancy flux from the strongest to the weakest of Earth's plumes shows good agreement with the total buoyancy fluxes extracted from geodynamical model runs (Figure S13 in Supporting Information S1).

$\Delta F_d^{\text{Geodyn}}$ results across the 22 geodynamical model runs have a mean $\Delta F_d^{\text{Geodyn}} = +0.004$, identical to $\Delta F_d^{\text{Geochem}}$ ($=+0.004$). The associated inter-run standard deviation for the geodynamical model is ± 0.004, a much narrower range than the inter-variant standard deviation of the geochemical model, which is ± 0.012. $\Delta f_{RC}^{\text{Geodyn}}$ results across geodynamical model runs have a mean $\Delta f_{RC}^{\text{Geodyn}} = +0.027$ with a standard deviation of ± 0.031. This value is partially controlled by outliers on the higher side, leading to a lower median of $\Delta f_{RC}^{\text{Geodyn}} = +0.019$. The inter-geodynamical model runs and inter-geochemical variants standard deviation for Δf_{RC} shows the opposite trend as for ΔF_d, with a narrow range for $\Delta f_{RC}^{\text{Geochem}}$ ($=\pm 0.006$) and a wide range for $\Delta f_{RC}^{\text{Geodyn}}$ ($=\pm 0.031$). The $\Delta f_{RC}^{\text{Geochem}}$ mean of $+0.015$ fits well within this larger range, and the geodynamical model median is within error of the geochemical model value.

The two classes of models thus show a good fit when considering their average ΔF_d and Δf_{RC} results. This correspondence is unlikely to be fortuitous as the results of both models are not random with respect to their inputs. In the geochemical model, F_d and f_{RC} are a product of the inversion and occupy a small and consistent fraction of the available ranges (Figures 3d and 4a). In the geodynamical model, trends are visible between input values for T_{CMB} and B and the resulting ΔF_d and Δf_{RC} (Figure 7). Rather, this fit suggests appropriate input ranges have been chosen for both classes of models. Interestingly, the variability of ΔF_d and Δf_{RC} is opposite, with near-constant Δf_{RC} and variable ΔF_d results in the geochemical model and with variable Δf_{RC} and near-constant ΔF_d results in the geodynamical model.

5.2. Reducing the Parameter Space of Both Classes of Models

The matching ΔF_d and Δf_{RC} averages of the geochemical model variants and geodynamical model runs, along with their opposite ranges, allow connecting the parameter space of both classes of models. Geochemical model variants can be rated based on how well their variable $\Delta F_d^{\text{Geochem}}$ match the well-defined $\Delta F_d^{\text{Geodyn}}$, and geodynamical model runs can be rated based on how well their variable $\Delta f_{RC}^{\text{Geodyn}}$ match the well-defined $\Delta f_{RC}^{\text{Geochem}}$.

Low CMB temperatures (3,400 and 3,600 K) lead to the best fits between $\Delta f_{RC}^{\text{Geodyn}}$ and the $\Delta f_{RC}^{\text{Geochem}}$ range (Figure 7). The reference case of 3,800 K leads to a good fit if $B = 0.66$, while a high CMB temperature of 4,000 K always lead to $\Delta f_{RC}^{\text{Geodyn}}$ values outside of the $\Delta f_{RC}^{\text{Geochem}}$ range. A buoyancy number $B = 0.22$ in the geodynamical model yields $\Delta f_{RC}^{\text{Geodyn}}$ results of ~ 0, never within the range of $\Delta f_{RC}^{\text{Geochem}}$. A buoyancy number $B = 0.44$ leads to a match with $\Delta f_{RC}^{\text{Geochem}}$ if the CMB temperature is $< 3{,}800$ K, but not in the reference case (3,800 K). A buoyancy number $B = 0.66$ shows the best match with $\Delta f_{RC}^{\text{Geochem}}$ at this CMB temperature. Comparison with the geochemical model thus suggests that a buoyancy number of $B = 0.22$ and a CMB temperature of 4,000 K are unrealistic. The presence of a dense primordial layer at the CMB in the geodynamical model leads on average to a slightly improved fit of $\Delta f_{RC}^{\text{Geodyn}}$ values with $\Delta f_{RC}^{\text{Geochem}}$ (Figure 7).

Only 7 of the 24 geochemical model variants yield a $\Delta F_d^{\text{Geochem}}$ within the range of $\Delta F_d^{\text{Geodyn}}$ (Figure 6). These are variants 00Gxx and variants 11GSS, 11SGG, and 11SGS. These three latter variants can be discarded due to their relatively low success rates (only 22%–65% of data cells can be reached by the model). In contrast, variants 00Gxx are highly successful with >97% of data cells reached by the model. These variants treat the formation of the DM source of recycled mafic material independently from that of the DM source of peridotite and decouple mafic crust formation from the second event of peridotite depletion. In these variants, PM melt-depletion to form DM occurs in the garnet stability field. The parameters distinguishing the four variants from each other are whether later melting events occur in the garnet or spinel stability field. As discussed in Section 3.2, the parametrization of these later melting events has only a minor impact on the model results.

5.3. Geological Implications and Perspectives

Our geochemical inversion model and the forward geodynamical mantle circulation model are fully separate and independent models, but their results are quantitatively consistent. This suggests that both modeling approaches are valid with realistic ranges for input parameters. Our estimates of the mantle's ΔF_d and Δf_{RC} values provide a useful theoretical basis for studies of Earth's thermochemical evolution. These values are also useful references for studies of plumes thermochemical buoyancy, as the compositional buoyancy of an upwelling plume in the upper mantle is a direct function of these two parameters. The presence of recycled crustal material in mantle plumes is a longstanding and widely accepted concept in geochemistry (e.g., Hofmann & White, 1982; Weis et al., 2023). This idea is both confirmed and quantified by our results with the geochemical model suggesting that the plume mantle contains on average 1.5% more recycled crust compared to the ridge mantle and the geodynamical model suggesting 1.9% (median result). Our results, however, also suggest that plume peridotite is slightly more depleted than ridge mantle peridotite, on average 0.4% more depleted in both models. This finding is at odds with the simple paradigm of enriched plumes, suggesting instead that the plume mantle is more chemically heterogeneous than the ridge mantle, with both excesses in peridotite melt-depletion and in the amount of recycled crust. An excess in plume peridotite depletion makes sense geologically as down-going slabs consist of both recycled oceanic crust and melt-depleted mantle lithosphere. Importantly, the presence of melt-depleted peridotite in mantle plumes increases their compositional buoyancy (Afonso & Schutt, 2012). The extent and temporal variability of peridotite melt-depletion in an upwelling plume is thus a parameter relevant to its upwelling dynamics. Depleted peridotite has indeed been invoked as a source of buoyancy for Iceland and Hawaii (Béguelin, Stracke, et al., 2025; Sanfilippo et al., 2024; Shorttle et al., 2014).

Our integration and subsequent reduction of both models' parameter space provides additional constraints on the thermochemical structure and history of the mantle (see Section 5.2). The success rate of geochemical model variants and the comparison of $\Delta F_d^{\text{Geochem}}$ results with the $\Delta F_d^{\text{Geodyn}}$ mean validate model variants 00Gxx. These variants require mantle processing and heterogeneities to be relatively old, with a mantle on average more primitive for the source of the recycled mafic material than for the rest of mantle peridotite prior to 2.5 Ga (Sections 3.2 and 3.3). Model variants with a more homogeneous DM at 2.5 Ga can model >94% of data cells but never match $\Delta F_d^{\text{Geodyn}}$ (Figure 6). Note that these old heterogeneities refer to the difference in origin between mafic material and mantle peridotite, and not to the modern spatial heterogeneities (e.g., plume vs. ridges). Mantle melting after 2.5 Ga must be treated separately as well, as linking mafic crust formation and peridotite depletion provides only a relatively low model success rate (11%–86% of cells). Our geochemical model results require DM formation to occur in the garnet stability field to match the robust $\Delta F_d^{\text{Geodyn}}$ value. DM formation in the spinel stability field leads to plume peridotite depletion in excess of what the geodynamical model results allow. This latter finding may however need to be confirmed by future geodynamical model runs with alternative initial compositional mixtures to further test the effect of this parameter on $\Delta F_d^{\text{Geodyn}}$ (see discussion in Text S3 of Supporting Information S1).

Comparing the variable $\Delta f_{\text{RC}}^{\text{Geodyn}}$ results to the robust $\Delta f_{\text{RC}}^{\text{Geochem}}$ value suggests that the CMB temperature is between 3,400 and 3,800 K. Our model comparison suggests that a temperature of 4,000 K can be excluded. The buoyancy number of upwelling recycled crust must be at least 0.44 with a best fit value of 0.66. A value of 0.22 leads to $\Delta f_{\text{RC}}^{\text{Geodyn}}$ values lower than what $\Delta f_{\text{RC}}^{\text{Geochem}}$ in the geochemical model allows, likely resulting from a more efficient rate of full mantle mixing. We also find that a dense primordial layer at the CMB, as modeled in the geodynamical model, leads to a better fit with the geochemical model.

Our geochemical model results suggest that recycled sediments make up only around 0.1% of the MORB and OIB mantle sources ($f_{\mathrm{Sed}} \cdot f_{\mathrm{RC}}$). This parameter does however explain the EM-type compositions (see Section 3.3). In a similar fashion, HIMU-type compositions reflect dehydration processes that only affect minute amounts of the bulk source (see Section 3.3). Consequently, an EM-HIMU endmember mixing paradigm is irrelevant to 99.9% of the source, and no link should be made between large scale density structures in the mantle, theorized or imaged through seismic tomography, and the first order geometry of the MORB-OIB radiogenic isotope systematics.

The time-integrated isotopic effects of source parameters relevant to mantle density (peridotite depletion F_d and amount of recycled crust f_{RC}) cannot be easily dissociated from those of processes with near insignificant effects on source density such as sediment recycling, oceanic crust alteration and dehydration. F_d and f_{RC} can therefore only be calculated from isotope systematics when non-magmatic effects have been carefully corrected. This means that outputting radiogenic isotope systematics directly from geodynamical models using tracers (radioactive and radiogenic isotopes) is of limited use. This is because sediment recycling, crustal alteration and dehydration cannot be integrated currently into the model and would have to be treated separately. The opposite approach we use here solves this issue as the full integrated parameter space linking isotope systematics to source parameters (magmatic and non-magmatic) can be explored statistically through billions of *Monte Carlo* simulations, while only 10–100s of geodynamical model runs can be produced over the course of an entire research project.

The good agreement between the compositional results of both classes of models demonstrates that our geochemical model is indeed sensitive to the most important compositional source parameters. It is however significantly less sensitive to chronological parameters. This is because the most chronologically sensitive isotope ratios, $^{206}Pb/^{204}Pb$, $^{207}Pb/^{204}Pb$, $^{208}Pb/^{204}Pb$, are also the systems depending on the most complex elemental cycling with many uncertainties on U-Th-Pb budgets during low-temperature processes and on the storage of these elements in the mantle. New constraints on this cycling will be key to enable a better modeling quantification of the residence time of recycled crust in the mantle and a more systematic understanding of the thermochemical evolution rate of terrestrial planets.

Conflict of Interest

The authors declare no conflicts of interest relevant to this study.

Data Availability Statement

The software used in the present study as well as the full geodynamical model and geochemical model raw data are available on *Zenodo* (Béguelin, Panton, et al., 2025; https://doi.org/10.5281/zenodo.15507390). No new geochemical data were generated in this study. Literature geochemical data were compiled from the *PetDB* and *GEOROC* databases as described in Section 2.3. Tables S3 and S4 contain the full literature data sets with original references.

Acknowledgments
This work was supported by the NERC Large Grant "Mantle Circulation Constrained (MC2): A multidisciplinary 4D Earth framework for understanding mantle upwellings" (Grant NE/T012633/1). Geodynamical model runs were conducted on ARCHER2, the UK's national high-performance supercomputer. We thank Simon Matthews and an anonymous reviewer for their helpful comments.

References

Afonso, J. C., & Schutt, D. L. (2012). The effects of polybaric partial melting on density and seismic velocities of mantle restites. *Lithos*, *134*, 289–303. https://doi.org/10.1016/j.lithos.2012.01.009

Ballmer, M. D., Houser, C., Hernlund, J. W., Wentzcovitch, R. M., & Hirose, K. (2017). Persistence of strong silica-enriched domains in the Earth's lower mantle. *Nature Geoscience*, *10*(3), 236–240. https://doi.org/10.1038/ngeo2898

Bao, X., Lithgow-Bertelloni, C. R., Jackson, M. G., & Romanowicz, B. (2022). On the relative temperatures of Earth's volcanic hotspots and mid-ocean ridges. *Science*, *375*(6576), 57–61. https://doi.org/10.1126/science.abj8944

Barry, T. L., Davies, J. H., Wolstencroft, M., Millar, I. L., Zhao, Z., Jian, P., et al. (2017). Whole-mantle convection with tectonic plates preserves long-term global patterns of upper mantle geochemistry. *Scientific Reports*, *7*(1), 1870. https://doi.org/10.1038/s41598-017-01816-y

Basch, V., Sanfilippo, A., Genske, F., Böhnke, M., Zanetti, A., & Stracke, A. (2025). Inefficient melt mixing below a fast-spreading ridge revealed by Hess Deep lower gabbros (ODP Leg 147 and IODP Expedition 345). *Science Advances*, *11*(16), eadu2044. https://doi.org/10.1126/sciadv.adu2044

Baumgardner, J. R. (1985). Three-dimensional treatment of convective flow in the Earth's mantle. *Journal of Statistical Physics*, *39*(5–6), 501–511. https://doi.org/10.1007/bf01008348

Baumgardner, J. R., & Frederickson, P. O. (1985). Icosahedral discretization of the two-sphere. *SIAM Journal on Numerical Analysis*, *22*(6), 1107–1115. https://doi.org/10.1137/0722066

Béguelin, P., Bizimis, M., Beier, C., & Turner, S. (2017). Rift–plume interaction reveals multiple generations of recycled oceanic crust in Azores lavas. *Geochimica et Cosmochimica Acta*, *218*, 132–152. https://doi.org/10.1016/j.gca.2017.09.015

Béguelin, P., Bizimis, M., McIntosh, E. C., Cousens, B., & Clague, D. A. (2019). Sources vs processes: Unraveling the compositional heterogeneity of rejuvenated-type Hawaiian magmas. *Earth and Planetary Science Letters*, *514*, 119–129. https://doi.org/10.1016/j.epsl.2019.03.011

Béguelin, P., Panton, J., Andersen, M., Elliott, T., Davies, H., Rodney, J., & Plimmer, A. (2025). Code for the article comparing geochemical and geodynamical models of plume and ridge mantle source composition. *Zenodo*. https://doi.org/10.5281/zenodo.15507390

Béguelin, P., Stracke, A., Ballmer, M. D., Huang, S., Willig, M., & Bizimis, M. (2025). Variations in Hawaiian plume flux controlled by ancient mantle depletion. *AGU Advances*, *6*(2), e2024AV001434. https://doi.org/10.1029/2024av001434

Beier, C., Stracke, A., & Haase, K. M. (2007). The peculiar geochemical signatures of São Miguel (Azores) lavas: Metasomatised or recycled mantle sources? *Earth and Planetary Science Letters*, *259*(1–2), 186–199. https://doi.org/10.1016/j.epsl.2007.04.038

Bizimis, M., Griselin, M., Lassiter, J. C., Salters, V. J., & Sen, G. (2007). Ancient recycled mantle lithosphere in the Hawaiian plume: Osmium–hafnium isotopic evidence from peridotite mantle xenoliths. *Earth and Planetary Science Letters*, *257*(1–2), 259–273. https://doi.org/10.1016/j.epsl.2007.02.036

Blichert-Toft, J., Frey, F. A., & Albarede, F. (1999). Hf isotope evidence for pelagic sediments in the source of Hawaiian basalts. *Science*, *285*(5429), 879–882. https://doi.org/10.1126/science.285.5429.879

Bolfan-Casanova, N. (2005). Water in the Earth's mantle. *Mineralogical Magazine*, *69*(3), 229–257. https://doi.org/10.1180/0026461056930248

Bower, D. J., Gurnis, M., & Seton, M. (2013). Lower mantle structure from paleogeographically constrained dynamic Earth models. *Geochemistry, Geophysics, Geosystems*, *14*(1), 44–63. https://doi.org/10.1029/2012gc004267

Brunelli, D., Cipriani, A., & Bonatti, E. (2018). Thermal effects of pyroxenites on mantle melting below mid-ocean ridges. *Nature Geoscience*, *11*(7), 520–525. https://doi.org/10.1038/s41561-018-0139-z

Bunge, H. P., & Baumgardner, J. R. (1995). Mantle convection modelling on parallel virtual machines. *Computers in Physics*, *9*(2), 207–215. https://doi.org/10.1063/1.168525

Bunge, H. P., Richards, M. A., & Baumgardner, J. R. (1995). A sensitivity study of three-dimensional spherical mantle convection at 10^8 Rayleigh number: Effects of depth-dependent viscosity, heating mode, and an endothermic phase change. *Journal of Geophysical Research*, *102*, 1191–12007.

Bunge, H.-P., Richards, M. A., & Baumgardner, J. R. (2002). Mantle circulation models with sequential data assimilation: Inferring present day mantle structure from platemotion histories. *Philosophical Transactions of the Royal Society of London, Series A: Mathematical, Physical and Engineering Sciences*, *360*(1800), 2545–2567. https://doi.org/10.1098/rsta.2002.1080

Bunge, H.-P., Richards, M. A., Lithgow-Bertelloni, C., Baumgardner, J. R., Grand, S. P., & Romanowicz, B. A. (1998). Time scales and heterogeneous structure in geodynamic Earth models. *Science*, *280*(5360), 91–95. https://doi.org/10.1126/science.280.5360.91

Byerly, B. L., & Lassiter, J. C. (2014). Isotopically ultradepleted domains in the convecting upper mantle: Implications for MORB petrogenesis. *Geology*, *42*(3), 203–206. https://doi.org/10.1130/g34757.1

Cai, R., Liu, J., Pearson, D. G., Giuliani, A., van Keken, P. E., & Oesch, S. (2023). Widespread PREMA in the upper mantle indicated by low-degree basaltic melts. *Nature Communications*, *14*(1), 8150. https://doi.org/10.1038/s41467-023-43845-4

Cawood, P. A., & Hawkesworth, C. J. (2019). Continental crustal volume, thickness and area, and their geodynamic implications. *Gondwana Research*, *66*, 116–125. https://doi.org/10.1016/j.gr.2018.11.001

Chauvel, C., Lewin, E., Carpentier, M., Arndt, N. T., & Marini, J. C. (2008). Role of recycled oceanic basalt and sediment in generating the Hf–Nd mantle array. *Nature Geoscience*, *1*(1), 64–67. https://doi.org/10.1038/ngeo.2007.51

Coltice, N., Gérault, M., & Ulvrová, M. (2017). A mantle convection perspective on global tectonics. *Earth-Science Reviews*, *165*, 120–150. https://doi.org/10.1016/j.earscirev.2016.11.006

Davies, D. R., Goes, S., Davies, J. H., Schuberth, B. S. A., Bunge, H. P., & Ritsema, J. (2012). Reconciling dynamic and seismic models of Earth's lower mantle: The dominant role of thermal heterogeneity. *Earth and Planetary Science Letters*, *353*, 253–269. https://doi.org/10.1016/j.epsl.2012.08.016

Davies, G. F., & Richards, M. A. (1992). Mantle convection. *The Journal of Geology*, *100*(2), 151–206.

Davies, J. H., Panton, J., Altoe, I., Andersen, M., Béguelin, P., Biggin, A., et al. (2025). How to assess similarities and differences between mantle circulation models and Earth using disparate independent observations. *Proceedings of the Royal Society A: Mathematical, Physical and Engineering Sciences*, *481*(2315). https://doi.org/10.1098/rspa.2024.0827

Dorn, C., Khan, A., Heng, K., Connolly, J. A., Alibert, Y., Benz, W., & Tackley, P. (2015). Can we constrain the interior structure of rocky exoplanets from mass and radius measurements? *Astronomy & Astrophysics*, *577*, A83. https://doi.org/10.1051/0004-6361/201424915

Eisele, J., Sharma, M., Galer, S. J., Blichert-Toft, J., Devey, C. W., & Hofmann, A. W. (2002). The role of sediment recycling in EM-1 inferred from Os, Pb, Hf, Nd, Sr isotope and trace element systematics of the Pitcairn hotspot. *Earth and Planetary Science Letters*, *196*(3–4), 197–212. https://doi.org/10.1016/s0012-821x(01)00601-x

Elliott, T., Blichert-Toft, J., Heumann, A., Koetsier, G., & Forjaz, V. (2007). The origin of enriched mantle beneath São Miguel, Azores. *Geochimica et Cosmochimica Acta*, *71*(1), 219–240. https://doi.org/10.1016/j.gca.2006.07.043

Ferrando, C., Borghini, G., Sani, C., Genske, F., Ligi, M., Stracke, A., & Sanfilippo, A. (2024). Deep segregation and crystallization of ultra-depleted melts in the sub-ridge mantle. *Chemical Geology*, *644*, 121840. https://doi.org/10.1016/j.chemgeo.2023.121840

Flament, N., Bodur, Ö. F., Williams, S. E., & Merdith, A. S. (2022). Assembly of the basal mantle structure beneath Africa. *Nature*, *603*(7903), 846–851. https://doi.org/10.1038/s41586-022-04538-y

French, S. W., & Romanowicz, B. (2015). Broad plumes rooted at the base of the Earth's mantle beneath major hotspots. *Nature*, *525*(7567), 95–99. https://doi.org/10.1038/nature14876

Frost, D. A., Avery, M. S., Buffett, B. A., Chidester, B. A., Deng, J., Dorfman, S. M., et al. (2022). Multidisciplinary constraints on the thermal-chemical boundary between Earth's core and mantle. *Geochemistry, Geophysics, Geosystems*, *23*(3), e2021GC009764. https://doi.org/10.1029/2021gc009764

Gale, A., Dalton, C. A., Langmuir, C. H., Su, Y., & Schilling, J. G. (2013). The mean composition of ocean ridge basalts. *Geochemistry, Geophysics, Geosystems*, *14*(3), 489–518.

Garnero, E. J., & McNamara, A. K. (2008). Structure and dynamics of Earth's lower mantle. *Science*, *320*(5876), 626–628. https://doi.org/10.1126/science.1148028

Guimond, C. M., Wang, H., Seidler, F., Sossi, P., Mahajan, A., & Shorttle, O. (2024). From stars to diverse mantles, melts, crusts, and atmospheres of rocky exoplanets. *Reviews in Mineralogy and Geochemistry*, *90*(1), 259–300. https://doi.org/10.2138/rmg.2024.90.08

Harris, C. R., Millman, K. J., Van Der Walt, S. J., Gommers, R., Virtanen, P., Cournapeau, D., et al. (2020). Array programming with NumPy. *Nature*, *585*(7825), 357–362. https://doi.org/10.1038/s41586-020-2649-2

Herzberg, C., Asimow, P. D., Arndt, N., Niu, Y., Lesher, C. M., Fitton, J. G., et al. (2007). Temperatures in ambient mantle and plumes: Constraints from basalts, picrites, and komatiites. *Geochemistry, Geophysics, Geosystems*, *8*(2). https://doi.org/10.1029/2006gc001390

Herzberg, C., Cabral, R. A., Jackson, M. G., Vidito, C., Day, J. M. D., & Hauri, E. H. (2014). Phantom Archean crust in Mangaia hotspot lavas and the meaning of heterogeneous mantle. *Earth and Planetary Science Letters*, *396*, 97–106. https://doi.org/10.1016/j.epsl.2014.03.065

Hirschmann, M., & Kohlstedt, D. (2012). Water in Earth's mantle. *Physics Today*, *65*(3), 40–45.

Hofmann, A. W. (1997). Mantle geochemistry: The message from oceanic volcanism. *Nature*, *385*(6613), 219–229. https://doi.org/10.1038/385219a0

Hofmann, A. W., & White, W. M. (1982). Mantle plumes from ancient oceanic crust. *Earth and Planetary Science Letters*, *57*(2), 421–436. https://doi.org/10.1016/0012-821x(82)90161-3

Hoggard, M. J., Parnell-Turner, R., & White, N. (2020). Hotspots and mantle plumes revisited: Towards reconciling the mantle heat transfer discrepancy. *Earth and Planetary Science Letters*, *542*, 116317. https://doi.org/10.1016/j.epsl.2020.116317

Hunter, J. D. (2007). Matplotlib: A 2D graphics environment. *Computing in Science & Engineering*, *9*(3), 90–95. https://doi.org/10.1109/mcse.2007.55

Ishii, T., Kojitani, H., & Akaogi, M. (2019). Phase relations of harzburgite and MORB up to the uppermost lower mantle conditions: Precise comparison with pyrolite by multisample cell high-pressure experiments with implication to dynamics of subducted slabs. *Journal of Geophysical Research: Solid Earth*, *124*(4), 3491–3507. https://doi.org/10.1029/2018jb016749

Israel, C., Boyet, M., Doucelance, R., Bonnand, P., Frossard, P., Auclair, D., & Bouvier, A. (2020). Formation of the Ce-Nd mantle array: Crustal extraction vs. recycling by subduction. *Earth and Planetary Science Letters*, *530*, 115941. https://doi.org/10.1016/j.epsl.2019.115941

Jones, R. E., van Keken, P. E., Hauri, E. H., Tucker, J. M., Vervoort, J., & Ballentine, C. J. (2019). Origins of the terrestrial Hf-Nd mantle array: Evidence from a combined geodynamical-geochemical approach. *Earth and Planetary Science Letters*, *518*, 26–39. https://doi.org/10.1016/j.epsl.2019.04.015

Kaufmann, G., & Lambeck, K. (2000). Mantle dynamics, postglacial rebound and the radial viscosity profile. *Physics of the Earth and Planetary Interiors*, *121*(3–4), 301–324. https://doi.org/10.1016/s0031-9201(00)00174-6

Korenaga, J. (2018). Crustal evolution and mantle dynamics through Earth history. *Philosophical Transactions of the Royal Society A: Mathematical, Physical and Engineering Sciences*, *376*(2132), 20170408. https://doi.org/10.1098/rsta.2017.0408

Kumari, S., Paul, D., & Stracke, A. (2016). Open system models of isotopic evolution in Earth's silicate reservoirs: Implications for crustal growth and mantle heterogeneity. *Geochimica et Cosmochimica Acta*, *195*, 142–157. https://doi.org/10.1016/j.gca.2016.09.011

Kumari, S., Paul, D., & Stracke, A. (2019). Constraints on Archean crust formation from open system models of Earth evolution. *Chemical Geology*, *530*, 119307. https://doi.org/10.1016/j.chemgeo.2019.119307

Li, W. R., Shorttle, O., Maclennan, J., Matthews, S., Zhang, Y., Namur, O., et al. (2025). Taking the temperature of ocean islands: A petrological approach. *Journal of Petrology*, *66*(5), egaf033. https://doi.org/10.1093/petrology/egaf033

McKinney, W. (2011). Pandas: A foundational Python library for data analysis and statistics. *Python for high performance and scientific computing*, *14*(9), 1–9.

Montelli, R., Nolet, G., Dahlen, F. A., & Masters, G. (2006). A catalogue of deep mantle plumes: New results from finite-frequency tomography. *Geochemistry, Geophysics, Geosystems*, *7*(11). https://doi.org/10.1029/2006gc001248

Müller, R. D., Flament, N., Cannon, J., Tetley, M. G., Williams, S. E., Cao, X., et al. (2022). A tectonic-rules-based mantle reference frame since 1 billion years ago–implications for supercontinent cycles and plate–mantle system evolution. *Solid Earth*, *13*(7), 1127–1159. https://doi.org/10.5194/se-13-1127-2022

Mulyukova, E., Steinberger, B., Dabrowski, M., & Sobolev, S. V. (2015). Survival of LLSVPs for billions of years in a vigorously convecting mantle: Replenishment and destruction of chemical anomaly. *Journal of Geophysical Research: Solid Earth*, *120*(5), 3824–3847. https://doi.org/10.1002/2014jb011688

Murphy, D. T., Brandon, A. D., Debaille, V., Burgess, R., & Ballentine, C. (2010). In search of a hidden long-term isolated sub-chondritic 142Nd/144Nd reservoir in the deep mantle: Implications for the Nd isotope systematics of the Earth. *Geochimica et Cosmochimica Acta*, *74*(2), 738–750. https://doi.org/10.1016/j.gca.2009.10.005

Niu, Y., & O'Hara, M. J. (2003). Origin of ocean island basalts: A new perspective from petrology, geochemistry, and mineral physics considerations. *Journal of Geophysical Research*, *108*(B4). https://doi.org/10.1029/2002jb002048

Noack, L., & Breuer, D. (2014). Plate tectonics on rocky exoplanets: Influence of initial conditions and mantle rheology. *Planetary and Space Science*, *98*, 41–49. https://doi.org/10.1016/j.pss.2013.06.020

Ohtani, E. (2005). Water in the mantle. *Elements*, *1*(1), 25–30. https://doi.org/10.2113/gselements.1.1.25

Panton, J., Davies, J. H., Elliott, T., Andersen, M., Porcelli, D., & Price, M. G. (2022). Investigating influences on the Pb Pseudo-Isochron using three-dimensional mantle convection models with a continental reservoir. *Geochemistry, Geophysics, Geosystems*, *23*(8), e2021GC010309. https://doi.org/10.1029/2021gc010309

Panton, J., Davies, J. H., Koelemeijer, P., Myhill, R., & Ritsema, J. (2025). Unique composition and evolutionary histories of large low velocity provinces. *Scientific Reports*, *15*(1), 4466. https://doi.org/10.1038/s41598-025-88931-3

Panton, J., Davies, J. H., & Myhill, R. (2023). The stability of dense oceanic crust near the core-mantle boundary. *Journal of Geophysical Research: Solid Earth*, *128*(2), e2022JB025610. https://doi.org/10.1029/2022jb025610

Peslier, A. H., Schönbächler, M., Busemann, H., & Karato, S. I. (2017). Water in the Earth's interior: Distribution and origin. *Space Science Reviews*, *212*(1–2), 743–810. https://doi.org/10.1007/s11214-017-0387-z

Plank, T., & Langmuir, C. H. (1998). The chemical composition of subducting sediment and its consequences for the crust and mantle. *Chemical Geology*, *145*(3–4), 325–394. https://doi.org/10.1016/s0009-2541(97)00150-2

Plimmer, A., Davies, J. H., & Panton, J. (2024). Investigating the effect of lithosphere thickness and viscosity on mantle dynamics throughout the supercontinent cycle. *Geochemistry, Geophysics, Geosystems*, *25*(11), e2024GC011688. https://doi.org/10.1029/2024gc011688

Putirka, K. (2008). Excess temperatures at ocean islands: Implications for mantle layering and convection. *Geology*, *36*(4), 283–286. https://doi.org/10.1130/g24615a.1

Putirka, K. D. (2024). Exoplanet mineralogy. *Reviews in Mineralogy and Geochemistry*, *90*(1), 199–257. https://doi.org/10.2138/rmg.2024.90.07

Ricolleau, A., Perrillat, J. P., Fiquet, G., Daniel, I., Matas, J., Addad, A., et al. (2010). Phase relations and equation of state of a natural MORB: Implications for the density profile of subducted oceanic crust in the Earth's lower mantle. *Journal of Geophysical Research*, *115*(B8). https://doi.org/10.1029/2009jb006709

Rudge, J. F., Maclennan, J., & Stracke, A. (2013). The geochemical consequences of mixing melts from a heterogeneous mantle. *Geochimica et Cosmochimica Acta*, *114*, 112–143. https://doi.org/10.1016/j.gca.2013.03.042

Rudnick, R. L., & Gao, S. (2003). Composition of the continental crust In: The Crust. In R. L. Rudnick (Ed.) (Vol. 3). *Treatise on Geochemistry*.

Rudolph, M. L., Moulik, P., & Lekić, V. (2020). Bayesian inference of mantle viscosity from whole-mantle density models. *Geochemistry, Geophysics, Geosystems*, *21*(11), e2020GC009335. https://doi.org/10.1029/2020gc009335

Salters, V. J., Blichert-Toft, J., Fekiacova, Z., Sachi-Kocher, A., & Bizimis, M. (2006). Isotope and trace element evidence for depleted lithosphere in the source of enriched Ko'olau basalts. *Contributions to Mineralogy and Petrology*, *151*(3), 297–312. https://doi.org/10.1007/s00410-005-0059-y

Salters, V. J., Mallick, S., Hart, S. R., Langmuir, C. E., & Stracke, A. (2011). Domains of depleted mantle: New evidence from hafnium and neodymium isotopes. *Geochemistry, Geophysics, Geosystems*, *12*(8). https://doi.org/10.1029/2011gc003617

Salters, V. J., & Stracke, A. (2004). Composition of the depleted mantle. *Geochemistry, Geophysics, Geosystems*, *5*(5). https://doi.org/10.1029/2003gc000597

Sanfilippo, A., Pandey, A., Akizawa, N., Poulaki, E., Cunningham, E., Bickert, M., et al. (2025). Heterogeneous Earth's mantle drilled at an embryonic ocean. *Nature Communications*, *16*(1), 2016. https://doi.org/10.1038/s41467-025-57121-0

Sanfilippo, A., Salters, V., Tribuzio, R., & Zanetti, A. (2019). Role of ancient, ultra-depleted mantle in Mid-Ocean-Ridge magmatism. *Earth and Planetary Science Letters*, *511*, 89–98. https://doi.org/10.1016/j.epsl.2019.01.018

Sanfilippo, A., Stracke, A., Genske, F., Scarani, S., Cuffaro, M., Basch, V., et al. (2024). Upwelling of melt-depleted mantle under Iceland. *Nature Geoscience*, *17*(10), 1–7. https://doi.org/10.1038/s41561-024-01532-z

Sani, C., Sanfilippo, A., Ferrando, C., Peyve, A. A., Skolotonev, S. G., Muccini, F., et al. (2020). Ultra-depleted melt refertilization of mantle peridotites in a large intra-transform domain (Doldrums Fracture Zone; 7–8°N, Mid Atlantic Ridge). *Lithos*, *374*, 105698. https://doi.org/10.1016/j.lithos.2020.105698

Sani, C., Sanfilippo, A., Skolotnev, S., Ligi, M., Genske, F., & Stracke, A. (2024). Sampling Earth's mantle at intra-transform spreading ridges. *Geochimica et Cosmochimica Acta*, *374*, 156–172. https://doi.org/10.1016/j.gca.2024.04.032

Shorttle, O., Maclennan, J., & Lambart, S. (2014). Quantifying lithological variability in the mantle. *Earth and Planetary Science Letters*, *395*, 24–40. https://doi.org/10.1016/j.epsl.2014.03.040

Stegman, D. R., Richards, M. A., & Baumgardner, J. R. (2002). Effects of depth-dependent viscosity and plate motions on maintaining a relatively uniform mid-ocean ridge basalt reservoir in whole mantle flow. *Journal of Geophysical Research*, *107*(B6), 8. https://doi.org/10.1029/2001jb000192

Stracke, A. (2021). A process-oriented approach to mantle geochemistry. *Chemical Geology*, *579*, 120350. https://doi.org/10.1016/j.chemgeo.2021.120350

Stracke, A., & Béguelin, P. (2024). Basalts record a limited extent of mantle depletion: Cause and chemical geodynamic implications. *Geochemical Perspectives Letters*, *32*, 21–26. https://doi.org/10.7185/geochemlet.2437

Stracke, A., Bizimis, M., & Salters, V. J. (2003). Recycling oceanic crust: Quantitative constraints. *Geochemistry, Geophysics, Geosystems*, *4*(3). https://doi.org/10.1029/2001gc000223

Stracke, A., & Bourdon, B. (2009). The importance of melt extraction for tracing mantle heterogeneity. *Geochimica et Cosmochimica Acta*, *73*(1), 218–238. https://doi.org/10.1016/j.gca.2008.10.015

Stracke, A., Genske, F., Berndt, J., & Koornneef, J. M. (2019). Ubiquitous ultra-depleted domains in Earth's mantle. *Nature Geoscience*, *12*(10), 851–855. https://doi.org/10.1038/s41561-019-0446-z

Stracke, A., Hofmann, A. W., & Hart, S. R. (2005). FOZO, HIMU, and the rest of the mantle zoo. *Geochemistry, Geophysics, Geosystems*, *6*(5). https://doi.org/10.1029/2004gc000824

Stracke, A., Willig, M., Genske, F., Béguelin, P., & Todd, E. (2022). Chemical geodynamics insights from a machine learning approach. *Geochemistry, Geophysics, Geosystems*, *23*(10), e2022GC010606. https://doi.org/10.1029/2022gc010606

Sun, S. S., & McDonough, W. F. (1989). Chemical and isotopic systematics of oceanic basalts: Implications for mantle composition and processes. *Geological Society*, *42*(1), 313–345. https://doi.org/10.1144/gsl.sp.1989.042.01.19

Van Heck, H. J., Davies, J. H., Elliott, T., & Porcelli, D. (2016). Global-scale modelling of melting and isotopic evolution of Earth's mantle: Melting modules for TERRA. *Geoscientific Model Development*, *9*(4), 1399–1411. https://doi.org/10.5194/gmd-9-1399-2016

Walter, M. J., & Trønnes, R. G. (2004). Early earth differentiation. *Earth and Planetary Science Letters*, *225*(3–4), 253–269.

Walzer, U., & Hendel, R. (2022). Mantle evolution and continental growth events. *Earth-Science Reviews*, *232*, 104130. https://doi.org/10.1016/j.earscirev.2022.104130

Wang, W., Xu, Y., Sun, D., Ni, S., Wentzcovitch, R., & Wu, Z. (2020). Velocity and density characteristics of subducted oceanic crust and the origin of lower-mantle heterogeneities. *Nature Communications*, *11*(1), 64. https://doi.org/10.1038/s41467-019-13720-2

Weis, D., Harpp, K. S., Harrison, L. N., Boyet, M., Chauvel, C., Farnetani, C. G., et al. (2023). Earth's mantle composition revealed by mantle plumes. *Nature Reviews Earth & Environment*, *4*(9), 604–625. https://doi.org/10.1038/s43017-023-00467-0

Westaway, R. (1993). Forces associated with mantle plumes. *Earth and Planetary Science Letters*, *119*(3), 331–348. https://doi.org/10.1016/0012-821x(93)90142-v

Willig, M., & Stracke, A. (2019). Earth's chondritic light rare earth element composition: Evidence from the Ce–Nd isotope systematics of chondrites and oceanic basalts. *Earth and Planetary Science Letters*, *509*, 55–65. https://doi.org/10.1016/j.epsl.2018.12.004

Willig, M., Stracke, A., Beier, C., & Salters, V. J. (2020). Constraints on mantle evolution from Ce-Nd-Hf isotope systematics. *Geochimica et Cosmochimica Acta*, *272*, 36–53. https://doi.org/10.1016/j.gca.2019.12.029

Workman, R. K., & Hart, S. R. (2005). Major and trace element composition of the Depleted MORB Mantle (DMM). *Earth and Planetary Science Letters*, *231*(1–2), 53–72. https://doi.org/10.1016/j.epsl.2004.12.005

Yang, W. S., & Baumgardner, J. R. (2000). A matrix-dependent transfer multigrid method for strongly variable viscosity infinite Prandtl number thermal convection. *Geophysical & Astrophysical Fluid Dynamics*, *92*(3–4), 151–195. https://doi.org/10.1080/03091920008203715

Zindler, A., & Hart, S. (1986). Chemical geodynamics. In *Annual review of earth and planetary sciences* (Vol. 14, pp. 493–571). Annual Reviews, Inc., 1986.

References From the Supporting Information

Bouvier, A., Vervoort, J. D., & Patchett, P. J. (2008). The Lu–Hf and Sm–Nd isotopic composition of CHUR: Constraints from unequilibrated chondrites and implications for the bulk composition of terrestrial planets. *Earth and Planetary Science Letters*, *273*(1–2), 48–57. https://doi.org/10.1016/j.epsl.2008.06.010

Kelley, K. A., Plank, T., Ludden, J., & Staudigel, H. (2003). Composition of altered oceanic crust at ODP Sites 801 and 1149. *Geochemistry, Geophysics, Geosystems*, *4*(6). https://doi.org/10.1029/2002gc000435

Kogiso, T., Tatsumi, Y., & Nakano, S. (1997). Trace element transport during dehydration processes in the subducted oceanic crust: 1. Experiments and implications for the origin of ocean island basalts. *Earth and Planetary Science Letters*, *148*(1–2), 193–205. https://doi.org/10.1016/s0012-821x(97)00018-6

Pedregosa, F., Varoquaux, G., Gramfort, A., Michel, V., Thirion, B., Grisel, O., & Duchesnay, É. (2011). Scikit-learn: Machine learning in Python. *Journal of Machine Learning Research*, *12*, 2825–2830.

Tatsumoto, M., Knight, R. J., & Allegre, C. J. (1973). Time differences in the formation of meteorites as determined from the ratio of lead-207 to lead-206. *Science*, *180*(4092), 1279–1283. https://doi.org/10.1126/science.180.4092.1279